Journal of Applied Mechanics

Brief Notes

A Brief Note is a short paper that presents a specific solution of technical interest in mechanics but which does not necessarily contain new general methods or results. A Brief Note should not exceed 1500 words *or equivalent* (a typical one-column figure or table is equivalent to 250 words; a one line equation to 30 words). Brief Notes will be subject to the usual review procedures prior to publication. After approval such Notes will be published as soon as possible. The Notes should be submitted to the Technical Editor of the JOURNAL OF APPLIED MECHANICS. Discussions on the Brief Notes should be addressed to the Editorial Department, ASME, United Engineering Center, Three Park Avenue, New York, NY 10016-5990, or to the Technical Editor of the JOURNAL OF APPLIED MECHANICS. Discussions on Brief Notes appearing in this issue will be accepted until two months after publication. Readers who need more time to prepare a Discussion should request an extension of the deadline from the Editorial Department.

On the Relation Between the *L*-Integral and the Bueckner Work-Conjugate Integral

J. P. Shi, X. H. Liu, and J. M. Li
Department of Engineering Mechanics, Xi'an University of Technology, 710048 Xi'an, China

A simple but inherent relation between the L-integral and the Bueckner work conjugate integral is deduced for crack problem in isotropic, anisotropic, and dissimilar materials, respectively. It is proved the L-integral, from the mathematical point of view as well as in principle, is arising from the Betti's reciprocal theorem. [S0021-8936(00)00103-3]

1 Introduction

Knowles and Sternberg [1] have shown that the L-integral is given by

$$L=\oint_{\Gamma} e_{3ij}(Wx_j n_i - T_i u_j - T_k u_{k,i} x_j)ds \tag{1}$$

where Γ is a closed contour in the $x_1=x$, $x_2=y$ plane surrounding a whole crack; W is the strain energy density, and T_i is the traction acting on the outer side of the Γ. The characteristics of the L-integral and the J_k-integral are different. It can be proven that the L-integral is a path-independent integral. We can also verify that the L-integral is independent of the selection of the coordinate system.

The Bueckner work-conjugate integral ([2]) was derived from the well-known Betti's reciprocal theorem, which could be formulated as follows:

$$I_\Gamma=\int_\Gamma (u_i^{(I)}\sigma_{ij}^{(II)}-u_i^{(II)}\sigma_{ij}^{(I)})n_j ds \quad (i,j=x,y) \tag{2}$$

where the superscripts (I) and (II) refer to two possible displacement-stress fields which satisfy the traction-free conditions on the crack faces. The property of the path-independent integral is proved by Bueckner using Betti's work reciprocal theorem, that is $I_\Gamma=I_C$.

2 Proof

For homogeneous isotropic materials, assume that the first possible displacement-stress field is induced by the following complex potentials $\varphi(z)$ and $\psi(z)$:

$$\begin{aligned}\varphi'(z)&=\frac{1}{\sqrt{z^2-a^2}}\sum_{k=1}^{+\infty}E_k z^k+\sum_{k=1}^{+\infty}F_k z^{k-1}\\ \psi'(z)&=\frac{1}{\sqrt{z^2-a^2}}\sum_{k=1}^{+\infty}E_k z^k-\sum_{k=1}^{+\infty}F_k z^{k-1}\end{aligned} \tag{3}$$

where E_k and F_k are complex coefficients which can be defined by remote conditions. Introduce a supplemental displacement-stress field defined by the following complex potentials $\varphi^{(II)}(z)$ and $\psi^{(II)}(z)$:

$$\begin{aligned}\varphi^{(II)}(z)&=-iz\varphi'(z)\\ \psi^{(II)}(z)&=-iz\psi'(z)+2i\overline{z}\varphi'(z).\end{aligned} \tag{4}$$

The corresponding displacement and stress components are derived as follows:

$$\begin{aligned}u_i^{(II)}&=yu_{i,x}-xu_{i,y}\\ \sigma_{ij}^{(II)}&=y\sigma_{ij,x}-x\sigma_{ij,y}+\frac{1}{2}\int\sigma_{ij,x}dy-\frac{1}{2}\int\sigma_{ij,y}dx \quad (i,j=1,2)\end{aligned} \tag{5}$$

where u_i and σ_{ij}, as the (I) field, are the displacement and stress components induced by Eq. (3). It can be examined that the stress $\sigma_{ij}^{(II)}$ satisfy the traction-free conditions on the crack faces. Substituting Eq. (5) and u_i and σ_{ij} into Eq. (2), we obtain

$$\begin{aligned}I_\Gamma=\int\Big[&u_i\sigma_{ij,x}y-u_i\sigma_{ij,y}x-u_{i,x}\sigma_{ij}y+u_{i,y}\sigma_{ij}x\\&+\frac{1}{2}u_i\int\sigma_{ij,x}dy-\frac{1}{2}u_i\int\sigma_{ij,y}dx\Big]n_j ds\end{aligned} \tag{6}$$

where $dx=-n_2 ds$, $dy=n_1 ds$.

Now, the $I_\Gamma-2L$ is examined. Utilizing the equilibrium conditions in plane problems and noting the integral terms $T_i u_i$, $\sigma_{ij}u_i$ and $u_i\int\sigma_{ij,x}dy$ have no contribution for $I_\Gamma-2L$ when $\rho\to 0$ (at the near of crack tip). Thus, $I_\Gamma-2L$ is equal to zero. We obtain

Contributed by the Applied Mechanics Division of THE AMERICAN SOCIETY OF MECHANICAL ENGINEERS for publication in the ASME JOURNAL OF APPLIED MECHANICS. Manuscript received by the ASME Applied Mechanics Division, June 6, 1999; final revision, January 21, 2000. Associate Technical Editor: J. T. Ju.

$$I_\Gamma = 2L. \tag{7}$$

Equation (7) shows that between the L-integral and the Bueckner work conjugate integral there is a simple but inherent relationship. We need not to know the obvious function expressions of complex potentials for the crack beforehand, but the traction-free conditions must be satisfied.

If there are two displacement-stress fields, namely, u_i, σ_{ij} and $u_i^{(II)}$, $\sigma_{ij}^{(II)}$, using the Betti's reciprocal theorem to the region bounded by crack borders, one can divide the contour C into C_L, C_R and C_+, C_-, where C_L, C_R are circles around the left and the right crack tips and C_+, C_- are the straight line along the upper and lower crack faces, respectively. Because the stresses are free on the crack faces, then $I_\Gamma = I_{CL} + I_{CR}$. In this case, if integrals I_{CL} and I_{CR} can be evaluated for some displacement-stress fields, then the path-independent integral I_Γ can also be defined and evaluated. If the displacement-stress fields are defined by Eqs. (3) and (4), we can deduce the following relationship between the L-integral and the stress intensity factors:

$$L = -\frac{3(\kappa-1)a}{4\mu}(K_{1L}K_{2L} + K_{1R}K_{2R}) \tag{8}$$

where $K_L = K_{1L} + iK_{2L}$, $K_R = K_{1R} + iK_{2R}$ are stress intensity factors at the left and the right crack tips, respectively. κ and μ are elastic constants.

3 Discussion

The complex potentials of the center crack, $\varphi_1(z), \omega_1(z), \varphi_2(z), \omega_2(z)$, were obtained by Chen and Shi [3] by using the same method obtained the eigenfunction expansion form by Rice [4] in interfacial cracks for dissimilar material. The stress and displacement fields that are obtained from these complex potentials satisfy the traction-free conditions on the crack faces and the continuous condition along the entire interface.

A supplemental displacement-stress field defined by the complex potentials $\varphi_1^{(II)}(z), \omega_1^{(II)}(z), \varphi_2^{(II)}(z), \omega_2^{(II)}$ is introduced. The relations between $\varphi_1^{(II)}(z), \omega_1^{(II)}(z), \varphi_2^{(II)}(z), \omega_2^{(II)}$ and $\varphi_1(z), \omega_1(z), \varphi_2(z), \omega_2(z)$ are analogous to Eq. (4).

In a similar manner, the displacement and stress of the (*II*) field are presented in Eq. (5). They satisfy the traction-free conditions on the crack faces also. The corresponding displacement and stress components will be substituted into Eq. (6). Note that the curve Γ can be divided into two sections: curve Γ_1 of the upper plane and the curve Γ_2 of the below plane. The deductions of Eqs. (6) to (7) relate to the equilibrium equations in plane problems and traction-free conditions only, but don't involve the material parameter. The process is the same as the above homogeneous isotropic material. Finally, we still obtain Eq. (7) in the interface crack, that is $I_\Gamma = 2L$.

Between L-integral and stress intensity factors there is the following relation:

$$L = -\left(\frac{\kappa_1 - 1}{\mu_1} + \frac{\kappa_2 - 1}{\mu_2}\right)\frac{3(K_{1L}K_{2L} + K_{1R}K_{2R})}{8\cosh^2(\pi\varepsilon)}a \tag{9}$$

where ε is ''oscillation index'' and $K_L = K_{1L} + iK_{2L}$, $K_R = K_{1R} + iK_{2R}$ are complex stress intensity factors at the left and the right crack-tips, respectively. They cannot be separated into the pure I model and II model; κ_1, μ_1 and κ_2, μ_2 stand for the material parameters of the upper and lower plane.

For anisotropy material, the Lekhenitski complex potential theory needs to be used ([5]). According to the need of the Bueckner work conjugate integral, the subsidiary stress-displacement fields, which represents (*II*) field, are

$$\varphi^{(II)}(z_1) = -iz_1\varphi'(z_1)$$
$$\psi^{(II)}(z_2) = -iz_2\psi'(z_2) + 2i\overline{z_2}\varphi'(z_1). \tag{10}$$

The stress fields caused by Eq. (10) satisfy the traction-free conditions. The relation between the (*II*) field and a physical stress field are analogous to Eq. (5).

By proceeding in the same manner as the isotropic case from Eq. (6) to Eq. (7), we draw a conclusion $I_\Gamma = 2L$.

It can be seen that a simple but inherent relation between the L-integral and the Bueckner work conjugate integral is right all along, although the characteristic of material is more complex than isotropic and the complex potentials in these two cases are more different with in isotropic.

4 Conclusions

Using the Bueckner work conjugate integral through introducing a special subsidiary stress-displacement field, one can render the L-integral. The relation between L-integral and the Bueckner work conjugate integral seems independent of the stress oscillatory singularities on the interface crack tips and the eigenroot in the anisotropy. It is found that the L-integral, from the mathematical point of view as well as in principle, is arising from the Betti's reciprocal theorem. This means that the Bueckner work conjugate integral is a more general path-independent integral than others are. Using the Bueckner integral through choosing a different subsidiary stress-displacement field could render any other path-independent integrals.

References

[1] Knowles, J. K., and Sternberg, E., 1972, ''On a Class of Conservation Laws in Linearized and Finite Elastostatics,'' Arch. Ration. Mech. Anal., **44**, pp. 187–211.

[2] Bueckner, H. F., 1973, *Mechanics of Fracture: Methods of Analysis and Solution of Crack Problems*, G. C. Sih, ed., Noordhoff, Leyden, pp. 239–314.

[3] Chen, Y. H., and Shi, J. P., 1998, ''On the Relation Between the *M*-integral and the Bueckner Work-Conjugate Integral,'' Acta Mech. Sin., **30**, pp. 495–502 (in Chinese).

[4] Rice, J. R., 1988, ''Elastic Fracture Mechanics Concepts for Interface Cracks,'' J. Appl. Mech., **55**, pp. 98–103.

[5] Sih, G. C., and Chen, E. P., 1981, ''Cracks in Composite Materials,'' Mech. Fracture, **6**, pp. 1–99.

A Note on the Driving Traction Acting on a Propagating Interface: Adiabatic and Non-Adiabatic Processes of a Continuum

R. Abeyaratne
Mem. ASME, Department of Mechanical Engineering, Massachusetts Institute of Technology, Cambridge, MA 02139

J. K. Knowles
Fellow ASME, Division of Engineering and Applied Sciences, California Institute of Technology, Pasadena, CA 91125

An expression for the driving traction on an interface is derived for an arbitrary continuum undergoing an arbitrary thermomechanical process which may or may not be adiabatic.

[S0021-8936(00)00403-7]

Contributed by the Applied Mechanics Division of THE AMERICAN SOCIETY OF MECHANICAL ENGINEERS for publication in the ASME JOURNAL OF APPLIED MECHANICS. Manuscript received by the ASME Applied Mechanics Division, July 30, 1997; final revision, Aug. 5, 1997. Associate Technical Editor: L. T. Wheeler.

1 Summary

In this note we derive an expression for the ''driving traction,'' or Eshelby force ([1]), acting on a propagating interface in a continuum. The interfaces that we have in mind might represent, for example, a shock wave or a boundary between two phases of a material, and the thermomechanical processes which the continuum is permitted to undergo may or may not be adiabatic. From the perspective of irreversible thermodynamics, the driving traction corresponds to a ''thermodynamic affinity''; see, for example, [2–4]. It plays a central role in modeling the kinetics of phase transformations by characterizing the rate of propagation of phase boundaries (e.g., see [5–8]).

The derivation sketched below makes no assumptions about the constitutive law for the continuum under consideration. When specialized to a thermoelastic material, the expression for the driving traction obtained here has certain similarities with the Legendre transform of the Helmholtz free-energy $\hat{\psi}(\mathbf{F},\theta)$ with respect to *both* the deformation gradient tensor $\mathbf{F}$ and the temperature θ, as well as with the Legendre transform of the internal energy $\hat{\varepsilon}(\mathbf{F},\eta)$ with respect to $\mathbf{F}$ and the specific entropy η.

The result derived here generalizes an earlier one which had been established for non-adiabatic processes ([9,10,5]). This former characterization of driving traction was not valid in adiabatic processes, and therefore did not, in particular, apply to shock waves in classical gas dynamics or to impact-induced rapidly moving phase boundaries in solids. A one-dimensional version of the present result was obtained in [11].

2 Momentum and Energy

Consider a body which occupies a region R in a reference configuration. Let $\mathbf{x}\in R$ denote the position of a particle in this configuration and let t denote time. Consider a thermomechanical process of this body on some time interval $[t_1,t_2]$ which is characterized by the motion $\mathbf{y}(\mathbf{x},t)$, body force per unit mass $\mathbf{b}(\mathbf{x},t)$, Piola-Kirchhoff stress $\boldsymbol{\sigma}(\mathbf{x},t)$, heat flux $\mathbf{q}(\mathbf{x},t)$, heat supply $r(\mathbf{x},t)$ and internal energy per unit mass $\varepsilon(\mathbf{x},t)$. Suppose that during this process $\mathbf{y}$ is continuous with piecewise continuous first and second derivatives on $R\times[t_1,t_2]$; $\mathbf{b}(\cdot,t)$ and $r(\cdot,t)$ are continuous on R; $\boldsymbol{\sigma}(\cdot,t)$ and $\mathbf{q}(\cdot,t)$ are piecewise continuous with piecewise continuous gradient on R; and ε is piecewise continuous with piecewise continuous first derivatives on $R\times[t_1,t_2]$. During this process, the usual balance laws of linear and angular momentum and the first law of thermodynamics require that for any subregion D,

$$\int_{\partial D}\boldsymbol{\sigma}\mathbf{n}\,dA+\int_D\rho\mathbf{b}\,dV=\frac{d}{dt}\int_D\rho\mathbf{v}\,dV, \tag{1}$$

$$\int_{\partial D}\mathbf{y}\times\boldsymbol{\sigma}\mathbf{n}\,dA+\int_D\mathbf{y}\times\rho\mathbf{b}\,dV=\frac{d}{dt}\int_D\mathbf{y}\times\rho\mathbf{v}\,dV, \tag{2}$$

$$\int_{\partial D}(\boldsymbol{\sigma}\mathbf{n}\cdot\mathbf{v}+\mathbf{q}\cdot\mathbf{n})dA+\int_D(\rho\mathbf{b}\cdot\mathbf{v}+\rho r)dV=\frac{d}{dt}\int_D\left(\frac{1}{2}\rho\mathbf{v}\cdot\mathbf{v}+\rho\varepsilon\right)dV. \tag{3}$$

Here $\mathbf{v}=\dot{\mathbf{y}}$ denotes particle velocity, $\rho(\mathbf{x})$ is the mass density in the reference configuration which is assumed to be continuous on R, and $\mathbf{n}$ is a unit outward normal vector on ∂D.

At a point in R at which the fields are smooth the balance laws (1)–(3) yield the usual field equations

$$\mathrm{Div}\,\boldsymbol{\sigma}+\rho\mathbf{b}=\rho\dot{\mathbf{v}}, \tag{4}$$

$$\boldsymbol{\sigma}\mathbf{F}^T=\mathbf{F}\boldsymbol{\sigma}^T, \tag{5}$$

$$\boldsymbol{\sigma}\cdot\dot{\mathbf{F}}+\mathrm{Div}\,\mathbf{q}+\rho r=\rho\dot{\varepsilon}, \tag{6}$$

where $\mathbf{F}=\mathrm{Grad}\,\mathbf{y}$ is the deformation gradient tensor.

Next, suppose that there is a surface S_t in R such that the fields $\mathbf{F}$, $\mathbf{v}$, $\mathbf{q}$, $\boldsymbol{\sigma}$ and ε suffer jump discontinuities across S_t while being continuous on either side of it. Such a surface may represent, for example, the Lagrangian image of a shock wave or an interface separating two material phases. Let $V_n\geqslant 0$ denote the normal velocity of propagation of this interface. We refer to the side into which V_n points as the positive side of S_t. For any field quantity $g(\mathbf{x},t)$ let $\overset{+}{g}$ and $\overline{g}$ denote the limiting values of g as a point on S_t is approached from its positive and negative side, respectively. Then, we let $[[g]]$ and $\langle g\rangle$ denote the jump and the average values of g on S_t:

$$[[g]]=\overset{+}{g}-\overline{g},\quad \langle g\rangle=\frac{1}{2}(\overset{+}{g}+\overline{g}). \tag{7}$$

At a point on S_t, the balance laws (1)–(3) yield the usual jump conditions

$$[[\boldsymbol{\sigma}\mathbf{n}]]+[[\rho\mathbf{v}]]V_n=0, \tag{8}$$

$$[[\boldsymbol{\sigma}\mathbf{n}\cdot\mathbf{v}]]+\left[\left[\rho\varepsilon+\frac{1}{2}\rho\mathbf{v}\cdot\mathbf{v}\right]\right]V_n+[[\mathbf{q}\cdot\mathbf{n}]]=0. \tag{9}$$

The energy jump condition (9) can be written in the following alternative form by making use of (8) and $[[\mathbf{v}]]+V_n[[\mathbf{Fn}]]=\mathbf{0}$ which follows from the continuity of the deformation (for algebraic details see, for example, [5]):

$$([[\rho\varepsilon]]-\langle\boldsymbol{\sigma}\rangle\cdot[[\mathbf{F}]])V_n=-[[\mathbf{q}\cdot\mathbf{n}]]. \tag{10}$$

3 Rate of Entropy Production

In order to address the second law of thermodynamics one must consider two additional fields, viz. the temperature $\theta(\mathbf{x},t)$ and the entropy per unit mass $\eta(\mathbf{x},t)$. Suppose that $\theta(\cdot,t)$ is piecewise continuous with a piecewise continuous gradient on R, and that η is piecewise continuous with piecewise continuous first derivatives on $R\times[t_1,t_2]$; θ and η are permitted to suffer jump discontinuities across S_t. The rate of entropy production associated with a subregion D is defined by

$$\Gamma=\frac{d}{dt}\int_D\rho\eta\,dV-\int_{\partial D}\frac{\mathbf{q}\cdot\mathbf{n}}{\theta}dA-\int_D\frac{\rho r}{\theta}dV, \tag{11}$$

and the second law of thermodynamics requires that $\Gamma\geqslant 0$ for all regions D and all processes. When the region D intersects the interface S_t one can rewrite (11) in the form

$$\Gamma=\int_D\left\{\rho\dot{\eta}-\mathrm{Div}\left(\frac{\mathbf{q}}{\theta}\right)-\frac{\rho r}{\theta}\right\}dV-\int_{S_t\cap D}\left\{[[\rho\eta]]V_n+\left[\left[\frac{\mathbf{q}\cdot\mathbf{n}}{\theta}\right]\right]\right\}dA \tag{12}$$

by carrying out a standard calculation; e.g. see page 116 of [12]. The first term in (12) represents the entropy production rate in the bulk of the body and the second term is associated with the moving interface. Let Γ_s denote the rate of entropy production due to the propagating surface:

$$\Gamma_s=-\int_{S_t}\left\{[[\rho\eta]]V_n+\left[\left[\frac{\mathbf{q}\cdot\mathbf{n}}{\theta}\right]\right]\right\}dA. \tag{13}$$

One finds by using (13) and (10), that Γ_s can be alternatively expressed as

$$\Gamma_s=\int_{S_t}\left\{\left[\left\langle\frac{1}{\theta}\right\rangle([[\rho\varepsilon]]-\langle\boldsymbol{\sigma}\rangle\cdot[[\mathbf{F}]])-[[\rho\eta]]\right]V_n+\langle\mathbf{q}\cdot\mathbf{n}\rangle\left[\left[\frac{1}{\theta}\right]\right]\right\}dA. \tag{14}$$

In an adiabatic process there is no heat transfer: $\mathbf{q}=\mathbf{0}$ and $r=0$. On the other hand if the process is not adiabatic, the typical heat conduction law, whatever it may be, involves Grad θ and therefore the partial differential equations resulting from using the constitutive relationships in the energy Eq. (6) involve (at least) the second spatial derivative of θ; thus, one usually requires the temperature to be continuous in non-adiabatic processes: $[[\theta]]=0$ on S_t. Thus in both the adiabatic and non-adiabatic cases one has $[[\theta]]\overset{\pm}{\mathbf{q}}=\mathbf{0}$ on S_t and therefore necessarily

$$\langle \mathbf{q}\cdot\mathbf{n}\rangle\left[\left[\frac{1}{\theta}\right]\right]=0 \quad \text{and} \quad \left(\left\langle\frac{1}{\theta}\right\rangle-\frac{1}{\langle\theta\rangle}\right)[[\mathbf{q}\cdot\mathbf{n}]]=0. \tag{15}$$

In view of this and (10), we can write Γ_s as

$$\Gamma_s=\int_{S_t}\frac{[[\rho\varepsilon]]-\langle\boldsymbol{\sigma}\rangle\cdot[[\mathbf{F}]]-\langle\theta\rangle[[\rho\eta]]}{\langle\theta\rangle}V_n\,dA, \tag{16}$$

or in terms of the Helmholtz free-energy $\psi=\varepsilon-\eta\theta$ as

$$\Gamma_s=\int_{S_t}\frac{[[\rho\psi]]-\langle\boldsymbol{\sigma}\rangle\cdot[[\mathbf{F}]]+\langle\rho\eta\rangle[[\theta]]}{\langle\theta\rangle}V_n\,dA. \tag{17}$$

4 Driving Traction

The rate of entropy production due to the propagating interface can be written as

$$\Gamma_s=\int_{S_t}\frac{fV_n}{\langle\theta\rangle}dA \tag{18}$$

where

$$\begin{aligned} f&=[[\rho\psi]]-\langle\boldsymbol{\sigma}\rangle\cdot[[\mathbf{F}]]+\langle\rho\eta\rangle[[\theta]]\\ &=[[\rho\varepsilon]]-\langle\boldsymbol{\sigma}\rangle\cdot[[\mathbf{F}]]-\langle\theta\rangle[[\rho\eta]] \end{aligned} \tag{19}$$

is called the driving traction or Eshelby force. The second law of thermodynamics requires that $fV_n\geqslant 0$ on S_t which specifies the direction in which the interface is permitted to move. This result is valid for any continuum undergoing an arbitrary thermomechanical process which may or may not be adiabatic. If the process is adiabatic, (19) and (10) yield $f=-\langle\theta\rangle[[\rho\eta]]$. If it is not adiabatic, (19) specializes to $f=[[\rho\psi]]-\langle\boldsymbol{\sigma}\rangle\cdot[[\mathbf{F}]]$.

In the special case of a thermoelastic material one has $\psi=\hat{\psi}(\mathbf{F},\theta)$ and the stress and entropy are given by the constitutive relationships $\boldsymbol{\sigma}=\rho\hat{\psi}_{\mathbf{F}}$, $\eta=-\hat{\psi}_\theta$. Equivalently one has $\varepsilon=\hat{\varepsilon}(\mathbf{F},\eta)$ with the stress and temperature given by $\boldsymbol{\sigma}=\rho\hat{\varepsilon}_{\mathbf{F}}$, $\theta=\hat{\varepsilon}_\eta$. Thus for a thermoelastic material (19) can be written as

$$\begin{aligned} f&=[[\rho\hat{\psi}]]-\langle\rho\hat{\psi}_{\mathbf{F}}\rangle\cdot[[\mathbf{F}]]-\langle\rho\hat{\psi}_\theta\rangle[[\theta]]\\ &=[[\rho\hat{\varepsilon}]]-\langle\rho\hat{\varepsilon}_{\mathbf{F}}\rangle\cdot[[\mathbf{F}]]-\langle\rho\hat{\varepsilon}_\eta\rangle[[\eta]] \end{aligned} \tag{20}$$

which is reminiscent of the Legendre transforms of $\rho\hat{\psi}(\mathbf{F},\theta)$ and $\rho\hat{\varepsilon}(\mathbf{F},\eta)$.

Acknowledgment

The results reported here were obtained in the course of research supported by the National Science Foundation.

References

[1] Eshelby, J. D., 1956, ''Continuum Theory of Lattice Defects,'' *Solid State Physics*, Vol. 3, F. Seitz and D. Turnbull, eds., Academic Press, San Diego, pp. 79–144.

[2] Callen, H. B., 1985, *Thermodynamics and an Introduction to Thermostatistics*, Second Ed., John Wiley and Sons, New York, Chapter 14.

[3] Kestin, J., 1968, *A Course on Thermodynamics*, Vol. II, McGraw-Hill, New York, Chapter 14.

[4] Truesdell, C., 1969, *Rational Thermodynamics* (Lecture 7), Springer-Verlag, New York.

[5] Abeyaratne, R., and Knowles, J. K., 1990, ''On the Driving Traction Acting on a Surface of Strain Discontinuity in a Continuum,'' J. Mech. Phys. Solids, **38**, pp. 345–360.

[6] Abeyaratne, R., and Knowles, J. K., 1991, ''Kinetic Relations and the Propagation of Phase Boundaries in Solids,'' Arch. Ration. Mech. Anal., **114**, pp. 119–154.

[7] Abeyaratne, R., Kim, S-J., and Knowles, J. K., 1994, ''A One-Dimensional Continuum Model for Shape-Memory Alloys,'' Int. J. Solids Struct., **31**, pp. 2229–2249.

[8] Rosakis, P., and Tsai, H., 1995, ''Dynamic Twinning Processes in Crystals,'' Int. J. Solids Struct., **32**, pp. 2711–2723.

[9] Heidug, W., and Lehner, F. K., 1985, ''Thermodynamics of Coherent Phase Transformations in Non-Hydrostatically Stressed Solids,'' Pure Appl. Geophys., **123**, pp. 91–98.

[10] Truskinovsky, L., 1985, ''Structure of an Isothermal Phase Discontinuity,'' Sov. Phys. Dokl., **30**, pp. 945–948.

[11] Abeyaratne, R., and Knowles, J. K., 1994, ''Dynamics of Propagating Phase Boundaries: Adiabatic Theory for Thermoelastic Solids,'' Physica D, **79**, pp. 269–288.

[12] Chadwick, P., 1976, *Continuum Mechanics*, John Wiley and Sons, New York.

Characterizing Damping and Restitution in Compliant Impacts via Modified K-V and Higher-Order Linear Viscoelastic Models

E. A. Butcher
Assoc. Mem. ASME, Department
of Mechanical Engineering,
University of Alaska, Fairbanks, AK 99775-5905

D. J. Segalman
Fellow ASME, Sandia National Laboratories,[1]
P.O. Box 5800,
MS 0847, Albuquerque, NM 87185-0847

1 Introduction

Time-domain models for compliant impacts have been widely used to model collision dynamics as finite-time events. The most common way to account for energy dissipation in the compliant impact model has been via the standard Kelvin-Voigt (K-V) viscoelastic model

$$F(t)=kx+c\dot{x} \tag{1}$$

in which the resulting equation of motion assumes the familiar linear form

$$\ddot{x}+2\zeta\omega_n\dot{x}+\omega_n^2x=0 \tag{2}$$

from vibration theory where $\omega_n=\sqrt{k/m}$ and $\zeta=c/(2\sqrt{km})$. The initial conditions $x(0)=0$ and $\dot{x}(0)=v_0$ yield the solution

$$x(t)=\frac{v_0}{\omega_d}\exp(-\zeta\omega_n t)\sin\omega_d t \tag{3}$$

where $\omega_d=\omega_n\sqrt{1-\zeta^2}$. If the impact duration is assumed to be a half-period of vibration associated with the damped frequency, then the exact restitution coefficient is obtained easily in terms of the dimensionless damping ratio as

[1]Sandia National Laboratories is a multiprogram laboratory operated by Sandia Corporation, A Lockheed Martin Company for the U.S. Department of Energy under Contract DE-ACO4, 94AL85000.

Contributed by the Applied Mechanics Division of THE AMERICAN SOCIETY OF MECHANICAL ENGINEERS for publication in the ASME JOURNAL OF APPLIED MECHANICS. Manuscript received by the ASME Applied Mechanics Division, August 25, 1998; final revision, February 10, 2000. Associate Technical Editor: V. K. Kinra.

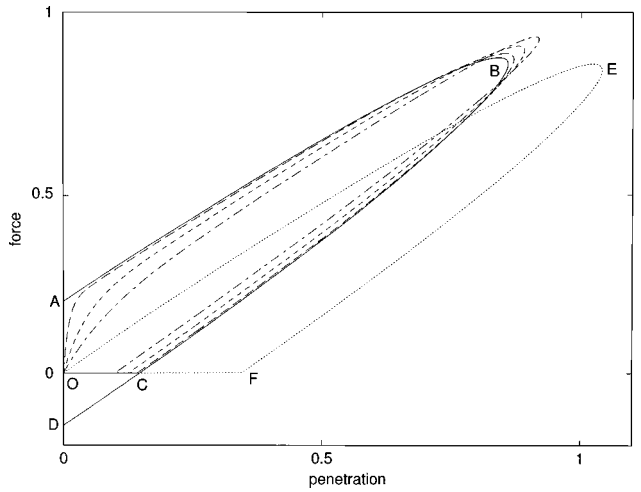

Fig. 1 Hysteresis diagrams for the Kelvin-Voigt (solid), Maxwell (dotted), and standard linear impact models with $\omega_n=1$ and $\zeta=0.1$ where $\eta=0.0$ (solid), 0.05 (long-dashed), 0.2 (short-dashed), and 0.4 (short-long-dashed). The modified K-V and standard linear models omit the tension at the conclusion of the restitution phase of impact.

$$e=-\frac{\dot{x}(t_r)}{\dot{x}(0)}=\exp\left(-\frac{\zeta\pi}{\sqrt{1-\zeta^2}}\right) \tag{4}$$

where $t_r=\pi/\omega_d$ is the release time ([1,2]). While the undamped collision is elastic, for critical damping or overdamping the collision is purely plastic. Another reason the half-period K-V model has been widely used is that Eq. (4) may easily be used to obtain the impact damping parameter c as

$$c=2|\ln e|\sqrt{\frac{km}{(\ln e)^2+\pi^2}} \tag{5}$$

in terms of an experimentally obtained restitution coefficient ([3]).

The energy E_L lost in the impact is

$$E_L=E_0(1-e^2)=E_0\left(1-\exp\left(-\frac{2\zeta\pi}{\sqrt{1-\zeta^2}}\right)\right) \tag{6}$$

where E_0 is the initial kinetic energy. This energy loss is represented in Fig. 1 by the area enclosed inside the hysteresis curve O-A-B-D-O. The peak elastic potential energy stored in the impact is

$$U=\frac{1}{2}kx_{\max}^2=E_0\exp\left(-\frac{2\zeta}{\sqrt{1-\zeta^2}}\tan^{-1}\frac{\sqrt{1-\zeta^2}}{\zeta}\right) \tag{7}$$

from which an equivalent linear damping ratio ζ_{eq} may be found via the loss factor $\eta=E_L/(2\pi U)$ as

$$\zeta_{eq}=\frac{\eta}{2}=\frac{1}{4\pi}\exp\left(\frac{2\zeta}{\sqrt{1-\zeta^2}}\tan^{-1}\frac{\sqrt{1-\zeta^2}}{\zeta}\right)\times\left(1-\exp\left(-\frac{2\zeta\pi}{\sqrt{1-\zeta^2}}\right)\right) \tag{8}$$

Thus the bilinear impact model may be replaced by an equivalent linear Kelvin-Voigt model with damping constant $c_{eq}=2\zeta_{eq}\sqrt{km}$ which dissipates E_L energy per period of vibration. This technique is often advantageous in vibratory impact problems.

Hunt and Crossley [4] noticed, however, that linear viscous damping in the K-V model gives an unrealistic hysteresis diagram for the impact force-deflection curve. Specifically, they noted that the parallel linear dashpot results in discontinuous force profiles at initial contact and release as well as a nonphysical tensile force applied during the end of the restitution phase. In order to eliminate this force discontinuity, they suggested a nonlinear damping function for use with the Hertzian stiffness model which complies with the expected boundary conditions of vanishing force at contact and release. Estimates of the corresponding restitution coefficient in terms of the model's damping parameters were made by the above authors and Herbert and McWhannell [5], who also noted that the effects of eliminating the force discontinuities include a more realistic frequency content in the impulse generated.

While other authors (e.g., [6,7]) have proposed different nonlinear models which also satisfy the expected boundary conditions, there have been few efforts to eliminate the force discontinuities in the K-V model while remaining within the framework of linear viscoelasticity. This paper attempts to help fill this gap. In contrast to using the various nonlinear models, this approach enables the associated damping and restitution to be characterized analytically without the need to approximate. First, the standard K-V model is reconsidered here under a different assumption regarding the restitution phase: that the mass releases when the *force* vanishes—*before* the initial contact location is reached. This approach was recently used by Luo and Hanagud [8] in order to improve the modeling and simulation of vibration absorbers with motion-limiting stops. In order also to guarantee that the force vanishes upon impact, higher-order viscoelastic (Maxwell and standard linear) models are implemented in which the boundary conditions in the force-displacement hysteresis curve are all satisfied and the force history is entirely continuous. A similar model for the impact surface has been utilized in a previous paper ([9]) in an effort to circumvent the previously mentioned discontinuities in the dynamic model of robotic manipulator collisions. Unlike these studies which were concerned with simulation, however, this paper presents analytical values of the restitution coefficient and related quantities for the viscoelastic models in terms of the dimensionless viscoelastic parameters. Hysteresis diagrams and restitution coefficients for each model are plotted and compared.

2 Modified K-V Model

In order to eliminate the tension in the K-V model, a better representation of the dynamics allows the mass to release when the net force vanishes. In Fig. 1, this occurs at point C. The resulting area of the hysteresis curve O-A-B-C-O (the energy loss) is thus smaller than that obtained using a half-period of vibration. Setting the force in Eq. (1) to zero, the release time is found as

$$t_r=\frac{1}{\omega_d}\tan^{-1}\left(\frac{2\zeta\sqrt{1-\zeta^2}}{2\zeta^2-1}\right) \tag{9}$$

which yields the restitution coefficient

$$e=\exp\left(-\frac{\zeta}{\sqrt{1-\zeta^2}}\tan^{-1}\left(\frac{2\zeta\sqrt{1-\zeta^2}}{2\zeta^2-1}\right)\right);\quad \zeta<1 \tag{10}$$

As $\zeta\to1, e\to\exp(-2)\approx0.14$ so that, unlike the half-period version, the impact is not perfectly plastic when the damping is critical. Instead, the nonzero restitution coefficient

$$e=\left(\frac{\zeta-\sqrt{\zeta^2-1}}{\zeta+\sqrt{\zeta^2-1}}\right)^{\zeta/\sqrt{\zeta^2-1}};\quad \zeta>1 \tag{11}$$

which matches Eq. (10) for $\zeta=1$ is obtained for overdamping. The energy lost in an impact is $E_L=E_0(1-e^2)$. Since the peak potential energy is given by Eq. (7) for $\zeta<1$ and by $U=E_0e$ for $\zeta>1$, the equivalent linear damping ratio may be obtained as

$$\zeta_{eq}=\begin{cases}\dfrac{1}{4\pi}\exp\left(\dfrac{2\zeta}{\sqrt{1-\zeta^2}}\tan^{-1}\dfrac{\sqrt{1-\zeta^2}}{\zeta}\right)\left(1-\exp\left(-\dfrac{2\zeta}{\sqrt{1-\zeta^2}}\tan^{-1}\left(\dfrac{2\zeta\sqrt{1-\zeta^2}}{2\zeta^2-1}\right)\right)\right); & \zeta<1\\ \dfrac{1}{2\pi}\sinh\left(\dfrac{-\zeta}{\sqrt{\zeta^2-1}}\ln\left(\dfrac{\zeta-\sqrt{\zeta^2-1}}{\zeta+\sqrt{\zeta^2-1}}\right)\right); & \zeta>1\end{cases} \tag{12}$$

from which an equivalent damping constant for use in vibratory impact is $c_{eq}=2\zeta_{eq}\sqrt{km}$. Although ζ_{eq} is less than in the half-period model, the difference remains less than 0.02 for $\zeta<1$. Thus, eliminating the force discontinuity at release results in a minimal decrease in equivalent damping.

3 Maxwell Model

The force discontinuity at impact cannot be eliminated in the K-V model due to the model's lack of an instantaneous elasticity. Instead, a higher-order viscoelastic model which portrays instantaneous elasticity may be utilized. The most basic of these is the Maxwell model in which the force-displacement relation is ([10])

$$F+\frac{c}{k}\dot{F}=c\dot{x}. \tag{13}$$

Equation (13) results in the third-order differential equation

$$\dddot{x}+2\zeta\omega_n\ddot{x}+\omega_n^2\dot{x}=0 \tag{14}$$

describing the impact dynamics where $\omega_n=\sqrt{k/m}$ and $\zeta=\sqrt{km}/(2c)$. The initial conditions $x(0)=0$, $\dot{x}(0)=v_0$, and $\ddot{x}(0)=0$ yield the solution

$$x(t)=\exp(-\zeta\omega_n t)\left(\frac{v_0}{\omega_d}(1-2\zeta^2)\sin\omega_d t-\frac{2\zeta v_0}{\omega_n}\cos\omega_d t\right)+\frac{2\zeta v_0}{\omega_n} \tag{15}$$

where $\omega_d=\omega_n\sqrt{1-\zeta^2}$.

As seen in Fig. 1 (hysteresis curve O-E-F-O), the discontinuity upon impact has been eliminated via the third initial condition. Furthermore, if release occurs when the force vanishes then all boundary conditions are satisfied. Since the release time is equivalent to a half-period ($t_r=\pi/\omega_d$), the restitution coefficient e and energy lost E_L are thus found to be equivalent to those obtained in the half-period K-V model. Thus as $\zeta\to1, e\to0$ and the collision becomes perfectly plastic. Since Eq. (4) also applies for the Maxwell model, the damping parameter is easily calculated in terms of the coefficient of restitution (as in the K-V model) as

$$c=\frac{\sqrt{km((\ln e)^2+\pi^2)}}{2|\ln e|}. \tag{16}$$

Because the spring and dashpot are in series, the peak elastic potential energy stored in the spring is found in terms of the maximum *force* as

$$U=\frac{1}{2}k\left(\frac{F_{\max}}{k}\right)^2=E_0\exp\left(-\frac{2\zeta}{\sqrt{1-\zeta^2}}\tan^{-1}\frac{\sqrt{1-\zeta^2}}{\zeta}\right). \tag{17}$$

The equivalent linear damping ratio, therefore, is also equivalent to that for the half-period K-V model so that the Maxwell impact model may be replaced by a linear K-V model with $c_{eq}=2\zeta_{eq}\sqrt{km}$ which dissipates E_L energy per period of vibration. It should be observed that, although certain quantities of the half-period K-V and Maxwell impact models are conveniently equivalent, their inherent physics are completely different as represented by the corresponding hysteresis curves.

4 Standard Linear Model

Another instantaneously elastic higher-order viscoelastic model which can be utilized is the standard linear model which consists of a K-V element (with spring constant k_2) in series with another spring k_1. The force-displacement relation is ([10])

$$(k_1+k_2)F+c\dot{F}=k_1k_2x+k_1c\dot{x}. \tag{18}$$

Equation (18) results in the third-order equation

$$\frac{2\zeta\eta}{\omega_n}\dddot{x}+\ddot{x}+2\zeta\omega_n\dot{x}+\omega_n^2x=0 \tag{19}$$

for the impact dynamics where $\omega_n=\sqrt{k_1k_2/((k_1+k_2)m)}$, while $\zeta=k_1c/(2(k_1+k_2)m\omega_n)$ and $\eta=k_2/(k_1+k_2)$ are the dimensionless viscoelastic parameters. In the limit as $k_1\to\infty$, then $\omega_n\to\sqrt{k_2/m}, 2\zeta\omega_n\to c/m, \eta\to0$, and the system becomes a K-V model with natural frequency ω_n and damping ratio ζ. Hence for $\eta\ll1$, Eq. (19) represents a perturbation of the standard K-V model (Eq. (2)). Although the exact solution and restitution coefficient are intractable in this model, an approximate closed-form solution may be obtained be means of a singular perturbation technique ([11]) in which the three roots α and $\beta\pm i\gamma$ are obtained to first order in η as

$$\alpha=-\frac{\omega_n}{2\zeta\eta}+2\zeta\omega_n+\eta(1-4\zeta^2)\zeta\omega_n$$
$$\beta=-\zeta\omega_n+\eta(1-4\zeta^2)\zeta\omega_n$$
$$\gamma=\omega_n\sqrt{1-\zeta^2}+\eta(3-4\zeta^2)\frac{\zeta^2}{\sqrt{1-\zeta^2}}\omega_n. \tag{20}$$

The perturbation series converges providing $\zeta<1/(2\sqrt{\eta})$.

The force-displacement hysteresis curves in Fig. 1 correspond to different values of the dimensionless parameter η. This parameter affects the model's instantaneous elasticity and can be adjusted to sufficiently ''smooth out'' the K-V force discontinuity at the origin. By allowing the mass to release at vanishing force, each of the force boundary conditions remain satisfied. Hence, for small values of η, the damping and restitution for this model are perturbations of those for the modified K-V model. The restitution coefficient was found for $\zeta<1$ to first order in η as

$$e=\exp\left(\left(-\frac{\zeta}{\sqrt{1-\zeta^2}}+\eta f_1(\zeta)\right)\left(\tan^{-1}\left(\frac{2\zeta\sqrt{1-\zeta^2}}{2\zeta^2-1}\right)+\eta f_2(\zeta)\right)\right) \tag{21}$$

where $f_1(\zeta)$ and $f_2(\zeta)$ were found to expand as $f_1(\zeta)=\zeta-\zeta^3/2+O(\zeta^5)$ and $f_2(\zeta)=2\zeta-3\zeta^3+O(\zeta^5)$. These approximations are accurate for small ζ and break down for ζ near unity. In order to verify the analytical expression in Eq. (21) using the expansions for $f_1(\zeta)$ and $f_2(\zeta)$, the restitution for different η values was also obtained numerically from the final velocity at release. It was found that the two results are practically identical for small values of both η and ζ. Finally, unlike the previous models considered, an equivalent linear damping ratio is not easily obtained for this model in terms of η and ζ.

5 Discussion

The restitution coefficients for each of the viscoelastic impact models are plotted as a function of ζ in Fig. 2 in which the half-

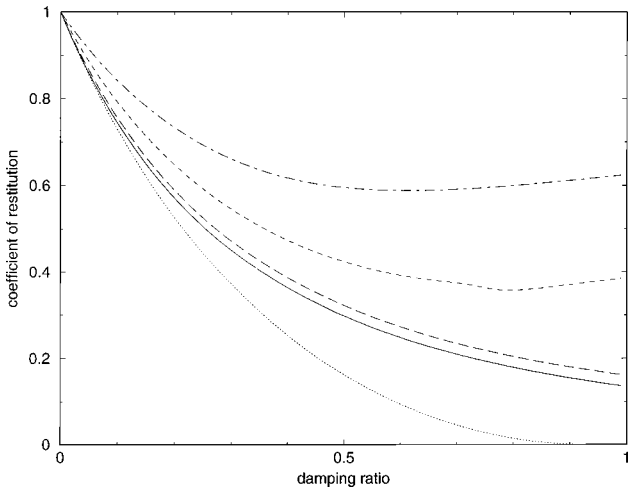

Fig. 2 Restitution coefficients for the half-period K-V and Maxwell models (dotted), modified K-V (solid), and standard linear impact model (numerical results) where η=0.0 (solid), 0.05 (long-dashed), 0.2 (short-dashed), and 0.4 (short-long-dashed)

period K-V and Maxwell results are identical. The numerical results for the standard linear model are shown for several values of η. The corresponding perturbation results (not shown) are essentially the same for small η and ζ. It is seen that the restitution coefficient of the half-period K-V and Maxwell models indeed vanishes as $\zeta \rightarrow 1$. Hence, a finite damping constant c_p may be associated with purely plastic impacts in these two models where $c_p = 2\sqrt{km}$ for K-V and $c_p = \sqrt{km}/2$ for Maxwell. In the modified K-V model, however, the restitution vanishes only as $\zeta \rightarrow \infty$ so that the impact can never be purely plastic. It is also seen that the modified K-V model has a restitution coefficient which is very close to that of the half-period K-V and Maxwell models for small damping ratios since the release times in these models for low damping are nearly the same. The advantages of analytically obtaining both the impact damping parameter (in terms of an experimentally obtained restitution coefficient) and the equivalent linear damping constant for use in vibroimpact, together with the even more significant fact that all of the force boundary conditions are satisfied, leads to the conclusion that the Maxwell model is an attractive choice for practical implementation in the modeling of dissipative compliant impacts. However, the standard linear model may also be helpful in ''smoothing out'' the K-V impact discontinuity. Especially if the impact duration is relatively long or there are additional static forces on the impact surface, the finite static deformation of this model is preferable to the fluid-like behavior of the Maxwell model. Furthermore, if the damping is small and the instantaneous stiffness is large, then the impact dynamics and restitution may be found as a perturbation of those for the modified K-V model as was done here. Finally, further work is needed to extend these results to general planar and three-dimensional collision theories and to include the use of kinetic and energetic restitution coefficients.

References

[1] Yigit, A. S., Ulsoy, A. G., and Scott, R. A., 1990, ''Dynamics of a Radially Rotating Beam With Impact, Part 1: Theoretical and Computational Model,'' ASME J. Vibr. Acoust., **112**, pp. 65–70.

[2] Brach, R. M., 1991, *Mechanical Impact Dynamics: Rigid Body Collisions*, John Wiley and Sons, New York.

[3] Brogliato, B., 1996, *Nonsmooth Impact Mechanics: Models, Dynamics, and Control*, Springer-Verlag, New York.

[4] Hunt, K. H., and Crossley, F. R. E., 1975, ''Coefficient of Restitution Interpreted as Damping in Vibroimpact,'' ASME J. Appl. Mech., **42**, pp. 440–445.

[5] Herbert, R. G., and McWhannell, D. C., 1977, ''Shape and Frequency Composition of Pulses From an Impact Pair,'' J. Eng. Ind., **99**, pp. 513–518.

[6] Lee, T. W., and Wang, A. C., 1983, ''On the Dynamics of Intermittent-Motion Mechanisms,'' ASME J. Mech. Des., **105**, pp. 534–540.

[7] Khulief, Y. A., and Shabana, A. A., 1987, ''A Continuous Force Model for the Impact Analysis of Flexible Multibody Systems,'' Mech. Mach. Theory, **22**, No. 3, pp. 213–224.

[8] Luo, H., and Hanagud, S., 1998, ''On the Dynamics of Vibration Absorbers With Motion-Limiting Stops,'' ASME J. Appl. Mech., **65**, pp. 223–233.

[9] Mills, J. K., and Nguyen, C. V., 1992, ''Robotic Manipulator Collisions: Modeling and Simulation,'' ASME J. Dyn. Syst., Meas., Control, **114**, pp. 650–659.

[10] Haddad, Y. M., 1995, *Viscoelasticity of Engineering Materials*, Chapman and Hall, New York.

[11] Nayfeh, A. H., 1981, *Introduction to Perturbation Techniques*, John Wiley and Sons, New York.

Finite-Amplitude Elastic Instability of Plane-Poiseuille Flow of Viscoelastic Fluids

R. E. Khayat
e-mail: rkhayat@eng.uwo.ca

N. Ashrafi

Department of Mechanical and Materials Engineering,
University of Western Ontario, London,
Ontario N6A 5B9, Canada

The purely elastic stability and bifurcation of the one-dimensional plane Poiseuille flow is determined for a large class of Oldroyd fluids with added viscosity, which typically represent polymer solutions composed of a Newtonian solvent and a polymeric solute. The problem is reduced to a nonlinear dynamical system using the Galerkin projection method. It is shown that elastic normal stress effects can be solely responsible for the destabilization of the base (Poiseuille) flow. It is found that the stability and bifurcation picture is dramatically influenced by the solvent-to-solute viscosity ratio, ε. As the flow deviates from the Newtonian limit and ε decreases below a critical value, the base flow loses its stability. Two static bifurcations emerge at two critical Weissenberg numbers, forming a closed diagram that widens as the level of elasticity increases. [S0021-8936(00)00703-0]

1 Introduction

While the problem of stability of plane-Poiseuille flow (PPF) has been extensively investigated for Newtonian fluids, relatively little attention has been devoted to the flow of viscoelastic fluids. The presence of viscoelasticity is expected to dramatically alter the stability and bifurcation picture in PPF, and yet no study has so far predicted the nonlinear bifurcation from the base flow. The presence of additional nonlinearities that are usually part of any realistic constitutive model ([1]) are expected to lead to the departure from the Newtonian picture. Similarly to the case of Taylor-Couette flow, there is experimental evidence that the base flow in a channel may lose its stability as a result of fluid elasticity inside the tube ([2]). This mechanism is now known as constitutive instability, as opposed to stick-slip induced instability. This mechanism of loss of stability should not be confounded with the short-wave instability due to a change in type of the field equations,

Contributed by the Applied Mechanics Division of THE AMERICAN SOCIETY OF MECHANICAL ENGINEERS for publication in the ASME JOURNAL OF APPLIED MECHANICS. Manuscript received by the ASME Applied Mechanics Division, April 28, 1999; final revision, July 27, 1999. Associate Technical Editor: A. K. Mal.

which is known as Hadamard instability ([3]). The emergence of surface instability at the exit of an extrusion die (sharkskin and melt fracture) keeps hinting at the possibility of a link with a hydrodynamic instability inside the channel, away and upstream from the exit ([4,5]). However, linear stability analyses of channel (Couette and Poiseuille) flows, using elementary constitutive models, such as Maxwell and Oldroyd-B fluids, failed to assert that the base flow may be linearly unstable when the level of elasticity (Weissenberg number) exceeds a critical level ([4,5]). More recent studies based on more generalized constitutive models of the Oldroyd class showed that the base flow in a channel can become unstable to small perturbations for some range of Weissenberg numbers ([6–8]). These generalized constitutive models display a nonmonotonic shear-stress/shear-rate curve. The range of instability coincides with the negative slope of the stress curve. However, only linear stability analyses were carried out.

The present study focuses on the nonlinear constitutive instability of the PPF of high-molecular-weight fluids. These fluids are typically composed of a Newtonian solvent and a polymeric solute. The Johnson-Segalman (JS) constitutive model is used, which is a highly nonlinear equation, and is one of the very few constitutive models that exhibit a nonmonotonic stress/shear-rate curve. It is thus expected that, while the presence of inertia and shear thinning alone can destabilize the flow, fluid elasticity or normal stresses will give rise to additional nonlinearities and coupling among the flow variables, making an already complex problem (due mainly to inertia) even more difficult to solve. Similarly to any flow in the transition regime, the PPF of viscoelastic fluids involves a continuous range of excited spatio-temporal scales. In order to assess the influence of the arbitrarily many smaller length and time scales on the flow, one would have to resort to the resolution of the flow at the small-scale level. This issue remains unresolved since, despite the great advances in storage and speed of modern computers, it will not be possible to resolve all of the continuous ranges of scales in the transition regime.

It is by now well established that dynamical systems can be a viable alternative to conventional numerical methods as one probes the nonlinear range of flow behavior ([9]). Dynamical systems are obtained using the Galerkin approximation. The velocity and stress components assume truncated Fourier or other orthogonal representations in space, depending on the boundary conditions. The expansion coefficients are functions of time alone, thus leading to a nonlinear system upon projection of the equations onto the various modes. The relative simplicity of dynamical systems, and the rich sequence of nonlinear flow phenomena exhibited by their solution, have been the major contributing factors to their widespread use as models for examining the onset of nonlinear behavior. The dynamical system approach has typically been used to handle simple flow configurations, and most particularly Newtonian flows. Recently, this approach has been attempted for non-Newtonian flows in thermal convection ([10–12]) and rotating flow ([13–17]). For Taylor-Couette flow, comparison was carried out with the experiments of Muller et al. [18], leading to excellent agreement ([15]). A modal expansion similar to that in [14,15] is used to solve the current problem.

2 Problem Formulation and Solution Procedure

Consider the plane channel (Poiseuille) flow of an incompressible viscoelastic fluid of density ρ, relaxation time λ, and viscosity η. In this study, only fluids that can be reasonably represented by a single relaxation time and constant viscosity are considered. The fluid considered here, is a polymer solution composed of a Newtonian solvent and a polymer solute of viscosities η_s and η_p, respectively. Therefore $\eta=\eta_s+\eta_p$. The velocity, time, space coordinates, pressure, and stress are nondimensionalized by d/λ, λ, d, $\eta_p U/d$ and η_p/λ, respectively. Here U is the maximum velocity of the base Poiseuille flow, and d is the gap between the two plates. There are three important similarity groups in the problem, namely, the Reynolds number, Re, the Weissenberg number, We, and the solvent-to-solute viscosity ratio, ε, which are given, respectively, by

$$\mathrm{Re}=\frac{d^2\rho}{\eta_p\lambda},\quad \mathrm{We}=\frac{U\lambda}{d},\quad \varepsilon=\frac{\eta_s}{\eta_p}. \tag{1}$$

The continuity and conservation of momentum equations for a general incompressible viscoelastic fluid are given in dimensionless form as

$$\nabla\cdot\mathbf{u}=0,\quad \mathrm{Re}\frac{d\mathbf{u}}{dt}=-\mathrm{We}\nabla p+\nabla\cdot\boldsymbol{\tau}+\varepsilon\nabla^2\mathbf{u} \tag{2}$$

where $\mathbf{u}$ is the velocity vector, p is the pressure, τ is the polymeric contribution of the stress tensor, t is the time, d/dt is the substantial derivative operator, and ∇ is the gradient operator. The constitutive equation adopted in this study belongs to the *Oldroyd* class of incompressible viscoelastic fluids:

$$\frac{d\boldsymbol{\tau}}{dt}-\left(1-\frac{\zeta}{2}\right)[(\nabla\mathbf{u})^t\cdot\boldsymbol{\tau}+\boldsymbol{\tau}\cdot\nabla\mathbf{u}]+\frac{\zeta}{2}[\nabla\mathbf{u}\cdot\boldsymbol{\tau}+\boldsymbol{\tau}\cdot(\nabla\mathbf{u})^t]$$
$$=\nabla\mathbf{u}+(\nabla\mathbf{u})^t \tag{3}$$

where $(\nabla\mathbf{u})^t$ denotes the transpose of $\nabla\mathbf{u}$. Equation (3) includes both lower and upper-convective terms. It is often referred to as the Johnson-Segalman model ([19]). Here $\zeta\in[0,2]$, which is a dimensionless material (slip) parameter. The value of ζ is a measure of the contribution of nonaffine motion to the shear tensor. For $\zeta=0$, the motion is affine and the Oldroyd-B model is recovered, whereas for $\zeta=2$, the motion is completely nonaffine and the model is reduced to the Oldroyd-Jaumann model ([4]). When $\zeta=0$ and $\eta_s=0$, the upper-convected Maxwell model is recovered.

If the x-axis is taken to lie halfway between the two plates, and y is the coordinate in the transverse direction, then the total shear stress corresponding to the base (Poiseuille) flow is given by

$$T^b_{xy}=\varepsilon\dot{\gamma}+\frac{\dot{\gamma}}{1+\zeta(2-\zeta)\dot{\gamma}^2}=\mathrm{We}\,y \tag{4}$$

where $\dot{\gamma}=du/dy$ is the shear rate and u is the velocity in the x-direction. Note that We is the dimensionless driving pressure gradient. Equation (4) is perhaps the most revealing result of the JS model. It reflects the possibility of a nonmonotonic behavior for the stress/shear-rate relation. Indeed, Fig. 1 shows the behavior of the shear stress, T^b_{xy}, as a function of $\dot{\gamma}$ for $\varepsilon\in[0,1]$ and ζ

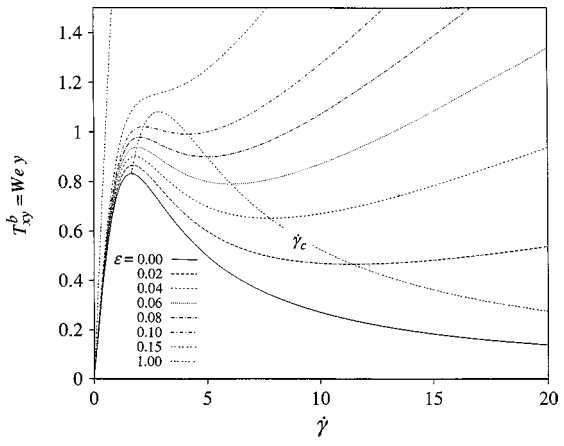

Fig. 1 Steady-state shear stress versus shear-rate curves for $\zeta=0.2$ and $\varepsilon\in[0,1]$. The loci of the two extrema are also shown, which join into one curve denoted here by $\dot{\gamma}_c$. The curves in the figure resemble the pressure/stretch-ratio related to the inflation of a Mooney-Rivlin material (see Fig. 2 in [20]).

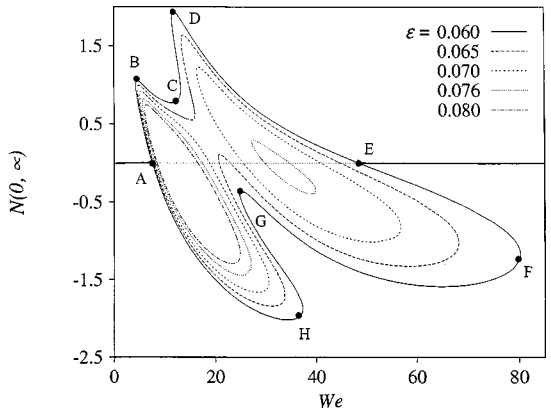

Fig. 2 Bifurcation diagrams for the normal stress difference, $N(0,\infty)$, at the center of the channel as function of We for $\zeta = 0.2$ and $\varepsilon \in [0.06, 0.08]$. The smallest diagram corresponds to the highest viscosity ratio, ε. As ε exceeds a critical level (in this case 1/8), the (closed) diagram reduces to zero, as the base flow is always stable. The branches AB, CD, EF, and GH of diagram $\varepsilon = 0.06$ are unstable, whereas the branches BC, DE, EF, FG, and HA are stable.

$=0.2$. The curve $\varepsilon = 1$ corresponds essentially to the Newtonian limit. For this value of the viscosity ratio, the elastic contribution to T^b_{xy} in expression (4) is negligible. In this case Newton's law of viscosity applies. The figure indicates that the stress curves lose monotonicity for $\varepsilon < 1/8$. Two extrema (a maximum and a minimum) appear, which tend to merge as ε increases, as indicated by the curve joining the loci of the extrema. The base flow is found to be unstable for the range of the stress curves with negative slope. This situation is reminiscent of the load/deformation behavior in elasticity. In the case of nonlinear inflation of a Mooney-Rivlin (hyperelastic) membrane, for instance, the pressure also exhibits a similar behavior as function of the stretch ratio for various Mooney constants ([20]). Upon comparison with the curves in Fig. 1, the curve $\varepsilon = 0$ is comparable to that of a Neo-Hookean solid, while the curve for a Newtonian fluid ($\varepsilon = 1$) is comparable to the curve of a Hookean solid (see Fig. 2 in [20]).

The solution of the system (1)–(2) is carried out using the Galerkin projection method. For one-dimensional disturbance along the channel (x-axis), the departure (from base flow) is reduced to the axial velocity, $u(y,t)$, normal stress difference, $N(y,t)$, and shear stress, $S(y,t)$. In this case, Eqs. (1)–(3) reduce to

$$\mathrm{Re}\, u_t = \varepsilon u_{yy} + S_y \tag{5a}$$

$$N_t = -N + 2(\mathrm{We}\, S + S u_y + S^b u_y). \tag{5b}$$

$$S_t = -S + u_y + a(\mathrm{We}\, N + N u_y + N^b u_y) \tag{5c}$$

where $a = \zeta(\zeta/2 - 1)$. Here $S^b = \dot\gamma/1 + \zeta(2-\zeta)\dot\gamma^2$ is the non-Newtonian contribution of the shear stress of the base flow, and $N^b = 2\dot\gamma^2/1 + \zeta(2-\zeta)\dot\gamma^2$ is the corresponding first normal stress difference. Note that a subscript in Eqs. (5) denotes partial differentiation. The flow departure is represented by series of Chandrasekhar functions, which satisfy the homogeneous (no-slip) boundary conditions ([15]). A judicious selection process and truncation level is applied for the choice of the various modes in order to ensure the physical and mathematical coherence of the final model.

3 Bifurcation and Stability Picture

While the (linear) stability picture is somewhat predictable, the bifurcation picture is far from being intuitively obvious. The bifurcation diagrams depend strongly on ε and ζ. We thus monitor the influence of the viscosity ratio by fixing the parameter ζ to 0.2 and varying ε. Figure 2 displays the resulting bifurcation diagrams in the (N, We) plane for $\varepsilon \in [0.06, 0.08]$. The figure shows the dependence of the steady-state normal stress difference, $N(0,\infty)$, at the center of the channel. Linear stability analysis asserts that, for large ε value ($>1/8$), the base flow is stable (to small perturbations) for any value of We. This situation corresponds to a monotonic shear-stress/shear-rate curve in Fig. 1. As ε decreases, two extrema appear in the stress curves in Fig. 1, entraining a loss of stability of the base flow in between. For each $\varepsilon > 1/8$, a closed bifurcation diagram emerges as depicted in Fig. 2, which shows a widening of the unstable range of We values as the viscosity ratio decreases.

Although the case $\varepsilon = 0.06$ will be discussed in detail below, we examine first the evolution of the bifurcation and stability picture as the flow deviates from close to the Newtonian limit (this limit is approached when the solvent-to-solute viscosity ratio, ε, is high). As ε decreases below a critical value, two static bifurcations emerge at two critical values, We_{c1} and We_{c2}, of the Weissenberg number as predicted by linear stability analysis. The two critical points coincide with points A and E for the $\varepsilon = 0.06$ diagram. The two bifurcating branches join over the unstable range to form a closed diagram. This is clearly illustrated for $\varepsilon = 0.08$; the closed diagram intersects the We axis at $\mathrm{We}_{c1} = 8.48$ and $\mathrm{We}_{c2} = 16.53$. As ε decreases further, the (closed) diagram widens, and another closed diagram appears as depicted in Fig. 2 for $\varepsilon = 0.076$. In this case, there are four critical values of the Weissenberg number that are present at 8.4, 17, 30, and 34.5. The second range of We values (30 to 34.5) corresponds to unstable base flow. A stable range exists between the two diagrams. As ε decreases further, the two diagrams grow, come in contact with one another, and finally merge to form a simply connected closed diagram as shown in Fig. 2 for $\varepsilon = 0.06$. In this case, the range of instability of the base flow becomes larger as it covers the values $7.54 < \mathrm{We} < 48.5$ (between A and E). The figure also indicates that the solution branch changes concavity, and presents regions alternating in stability.

In general, and as typically depicted by the $\varepsilon = 0.06$ diagram, there is an exchange of stability at the two critical points We_{c1} (A) and We_{c2} (E), with the base flow losing its stability at We_{c1} and regaining it at We_{c2}. However, the base flow is not always unconditionally stable for $\mathrm{We} < \mathrm{We}_{c1}$ and $\mathrm{We} > \mathrm{We}_{c2}$; simultaneously, the diagram $\varepsilon = 0.06$ is not always unconditionally stable for $\mathrm{We}_{c1} < \mathrm{We} < \mathrm{We}_{c2}$. We have indicated in Fig. 2 the various branches of alternating stability of the $\varepsilon = 0.06$ diagram. Thus, branches AB, CD, EF, and GH are unstable, while the branches BC, DE, FG, and HA are stable. Consequently, close to each critical point, just before We_{c1} and just after We_{c2}, there is a branch, BC and FG, respectively, to which the flow can converge if the perturbation is not small, similarly to what occurs in the vicinity of transcritical and subcritical bifurcations. Although there are stable and unstable nontrivial branches in the range $\mathrm{We}_{c1} < \mathrm{We} < \mathrm{We}_{c2}$, there is total loss of stability of the base flow. In this range, only nonlinear velocity profiles are stable. The stability of the branches at the two critical points was established numerically since linear stability analysis cannot be applied in the vicinity of the critical (nonhyperbolic fixed) points.

It is, perhaps, at this stage that one begins to connect the stability and bifurcation picture to physical reality. It is well known that in real systems, physical instabilities are observed when the flow rate and/or the level of elasticity are high. These instabilities are believed to be potentially responsible for the onset of surface roughness in extrusion [10]. If we note that the flow rate is controlled by We, and the level of elasticity controlled by both We and ε, then we can clearly observe that the trend shown in Fig. 2 confirms that both the flow rate and fluid elasticity are the determining factors behind the destabilization of the base flow. It is also well known that instabilities are suspected to set in after the Weissenberg number has reached a certain value. This is also

inferred from Fig. 2, as the diagram corresponding to $\varepsilon = 0.06$, for instance, indicates that the base flow is practically unstable for the whole range $We > 7.5$.

In summary, a nonlinear analysis is carried out to examine the onset of constitutive instability and bifurcation for polymer solutions. Only elastic effects, which lead to the well-known Weissenberg rod-climbing phenomenon, are responsible for the loss of stability of the base (Poiseuille) flow. The viscoelastic model used displays nonmonotonicity of the shear-stress/shear-rate curve, and belongs to the wider class of *Oldroyd* constitutive models that lead to the destabilization of channel flow. The bifurcation diagrams are obtained for the first time, and show how the secondary flow evolves as one deviates from the Newtonian limit. The bifurcation diagrams are always closed and widen in range as the solvent-to-solute viscosity decreases, thus reflecting the destabilization observed in practice as the level of elasticity increases. It is emphasized that the present stability and bifurcation picture corresponds to perturbations of infinite wavelength, which may not be the most dangerous modes. Only a higher-dimensional stability analysis can indicate whether the present findings are of physical relevance.

Acknowledgments

We would like thank J. M. Floryan (UWO) for helpful comments on the manuscript. This work is funded by the Natural Sciences and Engineering Research Council of Canada.

References

[1] Bird, R. B., Armstrong, R. C., and Hassager, O., 1987, *Dynamics of Polymeric Liquids*, Vol. 1, 2nd Ed., John Wiley and Sons, New York.

[2] Vinogradov, G. V., Malkin, A. Ya., Vanovskii, Yu G., Borisenkova, E. K., Yarlykov, B. V., and Berezheneya, G. V., 1972, J. Polym. Sci., Part A: Gen. Pap., **10**, p. 1061.

[3] Joseph, D. D., Renardy, M., and Saut, J. C., 1985, ''Hyperbolicity and Change of Type in the Flow of Viscoelastic Fluids,'' Arch. Ration. Mech. Anal., **87**, p. 213.

[4] Denn, M. M., 1990, ''Issues in Viscoelastic Fluid Mechanics,'' Annu. Rev. Fluid Mech., **22**, p. 13.

[5] Larson, R. G., 1992, ''Instabilities in Viscoelastic Flows,'' Rheol. Acta, **31**, p. 213.

[6] Kolkka, R. W., Malkus, D. S., Hansen, M. G., and Ierley, G. R., 1988, ''Spurt Phenomena of the Johnson-Segalman Fluid and Related Models,'' J. Non-Newtonian Fluid Mech., **29**, p. 303.

[7] Malkus, D. S., Nohel, J. A., and Plohr, B. J., 1990, ''Dynamics of Shear Flow of a Non-Newtonian Fluid,'' J. Comput. Phys., **87**, p. 464.

[8] Georgiou, G. C., and Vlassopoulos, D., 1998, ''On the Stability of the Simple Shear Flow of a Johnson-Segalman Fluid,'' J. Non-Newtonian Fluid Mech., **75**, p. 77.

[9] Sell, G. R., Foias, C., and Temam, R., 1993, *Turbulence in Fluid Flows: A Dynamical Systems Approach*, Springer-Verlag, New York.

[10] Khayat, R. E., 1994, ''Chaos and Overstability in the Thermal Convection of Viscoelastic Fluids,'' J. Non-Newtonian Fluid Mech., **53**, p. 227.

[11] Khayat, R. E., 1995, ''Nonlinear Overstability in the Thermal Convection of Viscoelastic Fluids,'' J. Non-Newtonian Fluid Mech., **58**, p. 331.

[12] Khayat, R. E., 1995, ''Fluid Elasticity and Transition of Chaos in Thermal Convection,'' Phys. Rev. E, **51**, p. 380.

[13] Avgousti, M., and Beris, A. N., 1993, ''Non-Axisymmetric Subcritical Bifurcations in Viscoelastic Taylor-Couette Flow,'' Proc. R. Soc. London, Ser. A, **A443**, p. 17.

[14] Khayat, R. E., 1995, ''Onset of Taylor Vortices and Chaos in Viscoelastic Fluids,'' Phys. Fluids A, **7**, p. 2191.

[15] Khayat, R. E., 1997, ''Low-Dimensional Approach to Nonlinear Overstability of Purely Elastic Taylor-Vortex Flow,'' Phys. Rev. Lett., **78**, p. 4918.

[16] Graham, M. D., 1998, ''Effect of Axial Flow on Viscoelastic Taylor-Couette Instability,'' J. Fluid Mech., **360**, p. 341.

[17] Ashrafi, N., and Khayat, R. E., 2000, ''Finite Amplitude Taylor-Vortex Flow of Weakly Shear-Thinning Fluids,'' Phys. Rev. E, **61**, p. 1455.

[18] Muller, S. J., Shaqfeh, E. S. J., and Larson, R. G., 1993, ''Experimental Study of the Onset of Oscillatory Instability in Viscoelastic Taylor-Couette Flow,'' J. Non-Newtonian Fluid Mech., **46**, p. 315.

[19] Johnson, M. W., and Segalman, D., 1977, ''A Model for Viscoelastic Fluid Behavior Which Allows Non-Affine Deformation,'' J. Non-Newtonian Fluid Mech., **2**, p. 278.

[20] Khayat, R. E., and Derdouri, A., 1994, ''Inflation of Hyperelastic Cylindrical Membranes as Applied to Blow Moulding, Part I. Axisymmetric Case,'' Int. J. Numer. Methods Eng., **37**, p. 3773.

In-Plane Gravity Loading of a Circular Membrane

R. O. Tejeda
Research Assistant

E. G. Lovell
Professor, Mem. ASME

R. L. Engelstad
Professor, Mem. ASME

Department of Mechanical Engineering, University of Wisconsin-Madison, Madison, WI 53706-1572

This paper develops the displacement field for a circular membrane which is statically loaded by gravity acting in its plane. Coupled to the displacements are the stress and strain distributions. The solution is applicable to the modeling of next generation lithographic masks, ion-beam projection lithography masks in particular. [S0021-8936(00)00803-5]

1 Introduction

In most engineering applications, the displacement, stress, and strain fields induced by gravity are negligible. However, in next generation (nonoptical) lithography masks used for semiconductor device fabrication, it is critical to predict and compensate for distortions which could potentially alter the quality of the microcircuit that is to be manufactured. Typically, the allowable error in a lithographic mask is only a fraction of the microcircuit's minimum feature size ([1]). Since ion-beam projection lithography (IPL) is targeting the production of sub-100 nm devices, displacements due to gravity can be significant.

An IPL mask is composed of a circular membrane that is supported by a relatively stiff frame and held in a vertical orientation during exposure ([2]). It is typically made of silicon with a diameter on the order of 200 mm and 3.0-μm thickness. If the mask is modeled as a circular membrane that is constrained on its perimeter by a rigid ring and subjected to in-plane gravitational loading (as shown in Fig. 1), it can be considered as a plane stress problem and solved directly by traditional applied elasticity methods. To the best of the authors' knowledge, a solution to this problem has not been presented in the elasticity literature.

2 Solution Development

The position of an arbitrary point on the membrane is defined by the polar coordinates (r, θ) with the origin taken at the center. All translational displacement components are constrained at the outside radius, R. In general, radial (u) and circumferential (v) displacements which arise from the loading of the membrane are related to the radial strain (ε_r), circumferential strain (ε_θ), and shear strain $(\gamma_{r\theta})$ by strain-displacement equations, and to radial normal stress (σ_r), circumferential normal stress (σ_θ), and shear stress $(\tau_{r\theta})$ by Hooke's law, i.e.,

$$\varepsilon_r = \frac{\partial u}{\partial r} = \frac{1}{E}(\sigma_r - \nu\sigma_\theta) \tag{1}$$

Contributed by the Applied Mechanics Division of THE AMERICAN SOCIETY OF MECHANICAL ENGINEERS for publication in the ASME JOURNAL OF APPLIED MECHANICS. Manuscript received by the ASME Applied Mechanics Division, Apr. 28, 1999; final revision, May 5, 2000. Associate Technical Editor: R. C. Benson.

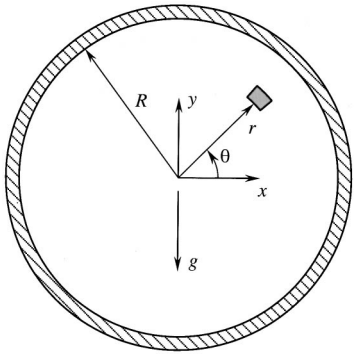

Fig. 1 In-plane gravity loading of a circular membrane

$$\varepsilon_\theta=\frac{u}{r}+\frac{1}{r}\frac{\partial v}{\partial\theta}=\frac{1}{E}(\sigma_\theta-\nu\sigma_r) \tag{2}$$

$$\gamma_{r\theta}=\frac{1}{r}\frac{\partial u}{\partial\theta}+\frac{\partial v}{\partial r}-\frac{v}{r}=\frac{2(1+\nu)}{E}\tau_{r\theta}. \tag{3}$$

Here, E is Young's modulus and ν is Poisson's ratio. Equilibrium of the shaded element shown in Fig. 1 requires that

$$\frac{\sigma_r-\sigma_\theta}{r}+\frac{\partial\sigma_r}{\partial r}+\frac{1}{r}\frac{\partial\tau_{r\theta}}{\partial\theta}-\rho g\sin\theta=0 \tag{4}$$

$$\frac{1}{r}\frac{\partial\sigma_\theta}{\partial\theta}+\frac{\partial\tau_{r\theta}}{\partial r}+\frac{2}{r}\tau_{r\theta}-\rho g\cos\theta=0 \tag{5}$$

where ρ and g are the material mass density and gravitational acceleration, respectively.

A solution form which uses Airy's stress function, ϕ, can be expressed as

$$\sigma_r=\frac{1}{r}\frac{\partial\phi}{\partial r}+\frac{1}{r^2}\frac{\partial^2\phi}{\partial\theta^2}+F(r,\theta) \tag{6}$$

$$\sigma_\theta=\frac{\partial^2\phi}{\partial r^2}+G(r,\theta) \tag{7}$$

$$\tau_{r\theta}=-\frac{\partial}{\partial r}\left(\frac{1}{r}\frac{\partial\phi}{\partial\theta}\right) \tag{8}$$

where $F(r,\theta)$ and $G(r,\theta)$ are arbitrary functions. Substituting Eqs. (6)–(8) into the equilibrium Eqs. (4) and (5) and subsequent integration yields

$$G(r,\theta)=\rho g r\sin\theta+G_2(r) \tag{9}$$

$$F(r,\theta)=\rho g r\sin\theta+\frac{F_2(r)}{r}+\frac{1}{r}\int G_2(r). \tag{10}$$

To preclude singular stresses, and without loss of generality, let $F_2(\theta)=G_2(r)=0$. Therefore,

$$\sigma_r=\frac{1}{r}\frac{\partial\phi}{\partial r}+\frac{1}{r^2}\frac{\partial^2\phi}{\partial\theta^2}+\rho g r\sin\theta \tag{11}$$

$$\sigma_\theta=\frac{\partial^2\phi}{\partial r^2}+\rho g r\sin\theta. \tag{12}$$

General forms of ϕ satisfying compatibility were originally given by Michell [3] for problems described in polar coordinates. From Timoshenko's ([4]) summary of this,

$$\begin{aligned}\phi=&a_0\log r+b_0r^2+c_0r^2\log r+d_0r^2\theta+a_0'\theta+\frac{a_1}{2}r\theta\sin\theta\\&+(b_1r^3+a_1'r^{-1}+b_1'r\log r)\cos\theta-\frac{c_1}{2}r\theta\cos\theta\\&+(d_1r^3+c_1'r^{-1}+d_1'r\log r)\sin\theta\\&+\sum_{n=2}^{\infty}(a_nr^n+b_nr^{n+2}+a_n'r^{-n}+b_n'r^{-n+2})\cos n\theta\\&+\sum_{n=2}^{\infty}(c_nr^n+d_nr^{n+2}+c_n'r^{-n}+d_n'r^{-n+2})\sin n\theta.\end{aligned} \tag{13}$$

A stress function which gives nonperiodic or singular stresses is not admissible. Therefore, all the terms except those with coefficients of b_0, b_1, d_1, a_n, b_n, c_n, and d_n will be dropped. So, for $n=2,3,4,\ldots$

$$\phi\propto r^n(\sin n\theta,\cos n\theta) \tag{14}$$

$$(\sigma_r,\sigma_\theta)\propto r^{n-2}(\sin n\theta,\cos n\theta) \tag{15}$$

$$\tau_{r\theta}\propto r^{n-2}(\cos n\theta,\sin n\theta). \tag{16}$$

On a circular edge, Eqs. (14)–(16) describe normal and shear stresses which vary harmonically. They are not necessary to solve the basic problem. Indeed, they may lead to displacements which cannot be zero at the boundary $r=R$. Thus, a solution may be constructed using relevant ϕ's established by Michell, plus additional terms associated with the gravitational body forces:

$$\phi=b_0r^2+b_1r^3\cos\theta+d_1r^3\sin\theta. \tag{17}$$

By the definition established in Eq. (8),

$$\tau_{r\theta}=2b_1r\sin\theta-2d_1r\cos\theta. \tag{18}$$

Due to the symmetric nature of the problem, $\tau_{r\theta}(r,\pi/2)=0$. Therefore, $b_1=0$. Similarly, Eqs. (11) and (12) show that

$$\sigma_r=2b_0+2d_1r\sin\theta+\rho g r\sin\theta \tag{19}$$

$$\sigma_\theta=2b_0+6d_1r\sin\theta+\rho g r\sin\theta. \tag{20}$$

Because it is associated with a hydrostatic loading such as uniform membrane prestress, b_0 will also be discarded. This leaves one unknown, d_1, which can be identified by noting that the circumferential normal strain is zero on the boundary, i.e., $\varepsilon_\theta(R,\theta)=0$. By using Eqs. (19), (20), and (2), this yields

$$d_1=\frac{-\rho g}{2}\frac{(1-\nu)}{(3-\nu)} \tag{21}$$

and the stresses can now be written in the form

$$\sigma_r=\frac{2\rho g}{(3-\nu)}r\sin\theta \tag{22}$$

$$\sigma_\theta=\frac{2\rho g\nu}{(3-\nu)}r\sin\theta \tag{23}$$

$$\tau_{r\theta}=\rho g\frac{(1-\nu)}{(3-\nu)}r\cos\theta. \tag{24}$$

Employing Eqs. (1)–(3), boundary conditions, and symmetry conditions gives the following strains and displacements in the membrane:

$$\varepsilon_r(r,\theta)=\frac{2\rho g}{E}\frac{(1-\nu^2)}{(3-\nu)}r\sin\theta \tag{25}$$

$$\varepsilon_\theta(r,\theta)=0 \tag{26}$$

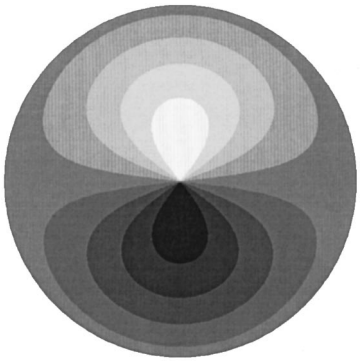

Fig. 2 Radial displacement contours. Range is $\pm\rho g(1-\nu^2)R^2/E(3-\nu)$.

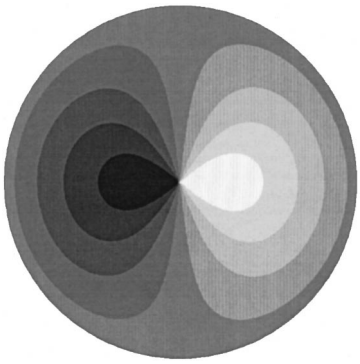

Fig. 3 Circumferential displacement contours. Range is $\pm\rho g(1-\nu^2)R^2/E(3-\nu)$.

$$\gamma_{r\theta}(r,\theta)=\frac{2\rho g}{E}\frac{(1-\nu^2)}{(3-\nu)}r\cos\theta \tag{27}$$

$$u=\frac{\rho g}{E}\frac{(1-\nu^2)}{(3-\nu)}(r^2-R^2)\sin\theta \tag{28}$$

$$v=\frac{\rho g}{E}\frac{(1-\nu^2)}{(3-\nu)}(r^2-R^2)\cos\theta. \tag{29}$$

The displacement component distributions given by Eqs. (28) and (29) are illustrated in Figs. 2 and 3.

Transformation of the stress components into an *x*-*y* coordinate system yields

$$\sigma_x=\frac{2\rho g\nu}{(3-\nu)}y \tag{30}$$

$$\sigma_y=\frac{2\rho g}{(3-\nu)}y \tag{31}$$

$$\tau_{xy}=\frac{\rho g(1-\nu)}{(3-\nu)}x; \tag{32}$$

where x and y are Cartesian coordinates, σ_x is the normal stress in the x-direction, σ_y is the normal stress in the y-direction, and τ_{xy} is the in-plane shear stress. As required, these stresses satisfy equilibrium equations in x and y, and the associated displacement components vanish on a circular boundary.

3 Conclusion

An elasticity solution for the in-plane gravitational loading of a circular membrane has been established. Stress, strain, and displacement fields satisfy symmetry, boundary conditions, equilibrium, compatibility for a linear elastic material, and are singularity-free.

The solution is useful for predicting the distortion of masks used in next generation lithography processes. It is particularly appropriate to modeling the ion-beam lithography mask, which consists of a large circular membrane supported by a frame or wafer ring while it is in a vertical orientation.

Acknowledgments

This research was supported by International SEMATECH, the Semiconductor Research Corporation (SRC), and the National Science Foundation Graduate Research Fellowship Program.

References

[1] Gross, G., 1997, ''Ion Projection Lithography: Next Generation Technology?,'' J. Vac. Sci. Technol., B**15**, No. 6, pp. 2136–2138.

[2] Tejeda, R., Engelstad, R., Lovell, E., and Berry, I., 1998, ''Analysis, Design, and Optimization of Ion-Beam Lithography Masks,'' Proc. SPIE, Emerging Lithographic Technologies II, **3331**, pp. 621–628.

[3] Michell, J. H., 1899, ''On the Direct Determination of Stress in an Elastic Solid, With Application to the Theory of Plates,'' Proc. London Math. Soc., **31**, pp. 100–124.

[4] Timoshenko, S. P., and Goodier, J. N., 1970, *Theory of Elasticity*, 3rd Ed., McGraw-Hill, New York, pp. 132–135.

Free Vibration of a Spinning Stepped Timoshenko Beam

S. D. Yu
Assistant Professor, Mem. ASME, Department of Mechanical Engineering, Ryerson Polytechnic University, 350 Victoria Street, Toronto, ON M5B 2K3, Canada

W. L. Cleghorn
Professor, Department of Mechanical and Industrial Engineering, University of Toronto, Five King's College Road, Toronto, ON M5S 3G8, Canada

The finite element method is employed in this paper to investigate free-vibration problems of a spinning stepped Timoshenko beam consisting of a series of uniform segments. Each uniform segment is considered a substructure which may be modeled using beam finite elements of uniform cross section. Assembly of global equation of motion of the entire beam is achieved using Lagrange's multiplier method. The natural frequencies and mode shapes are subsequently reduced with the help of linear transformations to a standard eigenvalue problem for which a set of natural frequencies and mode shapes may be easily obtained. Numerical results for an overhung stepped beam consisting of three uniform segments are obtained and presented as an illustrative example.

[S00021-8936(01)00101-5]

1 Introduction

In studying machine tool vibration during a turning cutting process, it is often necessary to conduct free-vibration analysis of

Contributed by the Applied Mechanics Division of THE AMERICAN SOCIETY OF MECHANICAL ENGINEERS for publication in the ASME JOURNAL OF APPLIED MECHANICS. Manuscript received and accepted by the ASME Applied Mechanics Division, Sept. 1, 1999; final revision, Apr. 10, 2000. Associate Technical Editor: N. C. Perkins.

spinning stepped shaft. Bauer [1] presented an analytical study of a rotating uniform Euler-Bernoulli beam with various combinations of simple boundary conditions. Lee et al. [2] studied the free vibration of a rotating Rayleigh shaft using the modal analysis approach and Galerkin's method. Katz et al. [3] investigated the dynamic responses of a uniform rotating shaft subjected to a moving load in the axial direction using both Rayleigh and Timoshenko beam theories. Zu and Han [4] presented analytical solutions for free vibration of a spinning uniform Timoshenko beam with all combinations of the three classical boundary conditions.

In this paper, free vibration of a rotating stepped Timoshenko beam is investigated using the finite element method. To enhance the accuracy of the computed eigenvalues and mode shapes, a three-node beam element, which permits the use of quintic polynomials as the interpolation function for both lateral displacements and bending angles, is utilized. For each of field variable, six nodal quantities—the variable and its derivative with respect to the axial coordinate at all three nodes are introduced to the element displacement vector. Two lateral deflections and two bending angles at each axial location need be defined in beam flexural vibration. Therefore, a three-node beam element has 24 nodal variables.

Use of the finite element method makes it possible to reduce the free-vibration problem of a spinning beam to a standard eigenvalue problem for which all eigenvalues and eigenvectors may be determined simultaneously. This is one advantage over the use of an analytical method in which eigenvalues are determined by searching for the roots of a characteristic equation. As an illustrative example, natural frequencies of an overhung stepped are obtained for several different spin rates.

2 Mathematical Procedure

In this section, the equations of motion of a stepped beam of circular cross section, as shown in Fig. 1, are presented using an inertial coordinate system. Parameters defining each segment are length, diameter, and axial coordinate of the left-most plane.

2.1 Governing Differential Equations for a Substructure. In modeling the stepped beam, each segment is considered a substructure. Within a substructure, the equations of motion may be written as ([3])

$$\left[\begin{bmatrix}\mathbf{L}_2 & \mathbf{0}\\ \mathbf{0} & \mathbf{L}_2\end{bmatrix}\frac{\partial^2}{\partial t^2}+2\Omega\begin{bmatrix}\mathbf{0} & \mathbf{L}_1\\ -\mathbf{L}_1 & \mathbf{0}\end{bmatrix}\frac{\partial}{\partial t}+\begin{bmatrix}\mathbf{L}_0 & \mathbf{0}\\ \mathbf{0} & \mathbf{L}_0\end{bmatrix}\right]\begin{Bmatrix}u_x\\ \psi_x\\ u_y\\ \psi_y\end{Bmatrix}=\begin{Bmatrix}0\\0\\0\\0\end{Bmatrix} \tag{1}$$

where u_x and u_y are lateral displacements of the beam centroid in the x and y directions, respectively; ψ_x and ψ_y are angles of rotation of the plane normal to the beam centroid, measured in the xoz and yoz coordinate planes, respectively; the three operator matrices are defined as

$$\mathbf{L}_2=\begin{bmatrix}\rho A & \mathbf{0}\\ \mathbf{0} & \rho I\end{bmatrix},\quad \mathbf{L}_1=\begin{bmatrix}\mathbf{0} & \mathbf{0}\\ \mathbf{0} & \rho I\end{bmatrix},\quad \mathbf{L}_0=\begin{bmatrix}-\kappa GA\dfrac{\partial^2}{\partial z^2} & \kappa GA\dfrac{\partial}{\partial z}\\ -\kappa GA\dfrac{\partial}{\partial z} & \kappa GA-EI\dfrac{\partial^2}{\partial z^2}\end{bmatrix}. \tag{2}$$

In Eq. (2), ρ is the volume mass density of the beam material; G is the shear modulus; E is the modulus of elasticity; A is the cross-sectional area; I is the second moment of area; κ is the shear correction factor (0.9 for solid circular cross section, [4]); Ω is the spin rate.

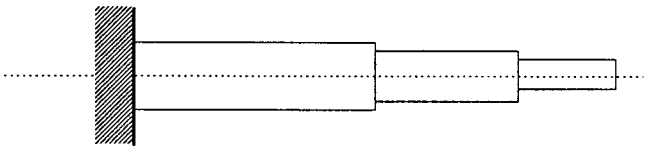

Fig. 1 An overhung stepped shaft

Assume that a uniform segment k is modeled using $N_{e,k}$ ($k=1,2,\ldots,N_s$) three-node beam elements. Within each element, the displacement vector $\{\mathbf{u}_e\}_k$ is related to the nodal displacement vector $\{\mathbf{q}_e\}_k$ by

$$\{\mathbf{u}_e\}_k=[\mathbf{N}_e(\xi)]\{\mathbf{q}_e\}_k \quad (0\leqslant\xi\leqslant l_e) \tag{3}$$

where ξ is the local coordinate; $\mathbf{N}_e(\xi)$ is the shape function matrix. The equations of motion of a uniform segment in terms of the nodal coordinate vector may be easily derived using the minimum potential energy principle or the Galerkin principle.

2.2 Assembly of Equations of Motion for the Stepped Beam. The global equations of motion for the entire beam may be formulated by enforcing continuity conditions across each interface between two adjacent substructures. The procedure is illustrated here for a single interface at node j with $z=z_j$. The four displacement and four force continuity conditions may be written in terms of the nodal displacements as

$$\begin{Bmatrix}u_x\\ \theta_x\\ \psi_x\\ k_x\\ u_y\\ \theta_y\\ \psi_y\\ k_y\end{Bmatrix}_{z=z_j^-}=\begin{bmatrix}1&0&0&0&0&0&0&0\\ 0&\alpha&1-\alpha&0&0&0&0&0\\ 0&0&1&0&0&0&0&0\\ 0&0&0&\beta&0&0&0&0\\ 0&0&0&1&0&0&0&0\\ 0&0&0&0&0&\alpha&1-\alpha&0\\ 0&0&0&0&0&0&1&0\\ 0&0&0&0&0&0&0&\beta\end{bmatrix}\times\begin{Bmatrix}u_x\\ \theta_x\\ \psi_x\\ k_x\\ u_y\\ \theta_y\\ \psi_y\\ k_y\end{Bmatrix}_{z=z_j^+}=\mathbf{C}_j\begin{Bmatrix}u_x\\ \theta_x\\ \psi_x\\ k_x\\ u_y\\ \theta_y\\ \psi_y\\ k_y\end{Bmatrix}_{z=z_j^+} \tag{4}$$

where α and β are the shear rigidity ratio and the bending rigidity ratio, defined as

$$\alpha=\frac{(\kappa GA)_1}{(\kappa GA)_2},\quad \beta=\frac{(EI)_1}{(EI)_2}. \tag{5}$$

The continuity conditions may be implemented into the global equations of motion using the Lagrange multiplier method ([5]). The final equations of motion of a stepped beam may be written as

$$[\mathbf{M}]\{\ddot{\mathbf{q}}\}+[\mathbf{G}]\{\dot{\mathbf{q}}\}+[\mathbf{K}]\{\mathbf{q}\}=\mathbf{0} \tag{6}$$

where the global mass, gyroscopic and stiffness matrices for the entire stepped beam may be formulated from the corresponding matrices for substructures and constraint matrices $\mathbf{C}_j$. For example, the global mass matrix for a three-segment stepped beam is

$$[\mathbf{M}]=\begin{bmatrix} \mathbf{M}_{11}^1 & \mathbf{M}_{12}^1 & \mathbf{0} & \mathbf{0} & \mathbf{0} \\ \mathbf{M}_{21}^1 & \mathbf{M}_{22}^1+\mathbf{C}_1^T\mathbf{M}_{11}^2\mathbf{C}_1 & \mathbf{C}_1^T\mathbf{M}_{12}^2 & \mathbf{M}_{13}^2 & \mathbf{0} \\ \mathbf{0} & \mathbf{M}_{21}^2\mathbf{C}_1 & \mathbf{M}_{22}^2 & \mathbf{M}_{23}^2 & \mathbf{0} \\ \mathbf{0} & \mathbf{M}_{31}^2 & \mathbf{M}_{32}^2 & \mathbf{M}_{33}^2+\mathbf{C}_2^T\mathbf{M}_{11}^3\mathbf{C}_2 & \mathbf{C}_2^T\mathbf{M}_{12}^3 \\ \mathbf{0} & \mathbf{0} & \mathbf{0} & \mathbf{M}_{21}^3\mathbf{C}_2 & \mathbf{M}_{22}^3 \end{bmatrix}.$$

2.3 Boundary Conditions. The global equations of motion of a stepped beam may be readily modified to account for boundary conditions at the ends using the penalty approach. In this paper, an overhung shaft clamped at one end and free at the other is investigated.

3 Standard Eigenvalue Problem

One of the most important tasks in free-vibration analysis is to determine the natural frequencies and mode shapes described by a system of homogeneous second-order differential equations and boundary conditions at the ends of a beam. To utilize commercial routines for eigenanalysis, the second-order system may be replaced by the following equivalent first-order system

$$\mathbf{A}\dot{\mathbf{x}}=\mathbf{B}\mathbf{x} \tag{7}$$

where coefficient matrices **A** and **B** may be obtained from matrices **M**, **K**, and **G**.

Natural frequencies and mode shapes of a spinning Timoshenko beam may then be reduced to seeking λ and **X** satisfying

$$\mathbf{A}\mathbf{X}=\frac{1}{\lambda}\mathbf{B}\mathbf{X}. \tag{8}$$

4 Numerical Results

Values of the material and geometric properties of a three segment stepped beam under investigation are given in Table 1. Table 2 provides values of natural frequencies of an overhung three segment stepped beam shown in Fig. 1. Five different spin rates are considered. For the case of zero spin rate, natural frequencies have matched pairs. For a nonzero spin rate, there are two natural frequencies developed around each at-rest value. One is associated with the forward precession mode; the other is associated with the backward precession mode.

Table 1 Material and geometric properties of a stepped spinning beam

	Geometric Properties			Material Properties		
	L_k (m)	d_k (m)	κ_k	E_k (GPa)	G_k (GPa)	ρ_k (kg/m^3)
Segment 1	0.3	0.191	0.9	207	77.6	7,700
Segment 2	0.3	0.150	0.9	207	77.6	7,700
Segment 3	0.4	0.100	0.9	207	77.6	7,700

Table 2 The first six natural frequencies of an overhung stepped beam

	Rotational Speed (rad/s)				
Modes	0	2,500	5,000	7,500	10,000
1a	1242.2	1224.2	1206.3	1188.7	1171.3
1b	1242.2	1260.4	1278.9	1297.5	1316.4
2a	3932.0	3867.3	3803.1	3739.3	3676.2
2b	3932.0	3997.1	4062.6	4128.4	4194.4
3a	9362.8	9216.9	9071.9	8928.1	8785.4
3b	9362.8	9509.5	9656.7	9804.5	9952.4

5 Conclusions

This paper presents a finite element analysis of free vibration of a spinning stepped Timoshenko beam. Through use of the Lagrange multipliers method, both displacement continuity and force equilibrium conditions are satisfied at the interfaces of joining substructures. Because of the use of higher-order beam finite elements for each substructure, highly accurate natural frequencies of a stepped beam of any desired mode may be obtained.

References

[1] Bauer, H. F., 1980, ''Vibration of a Rotating Uniform Beam, Part 1: Orientation in the Axis of Rotation,'' J. Sound Vib., **72**, No. 2, pp. 177–189.

[2] Lee, C. W., Katz, R., Ulsoy, A. G., and Scott, R. A., 1988, ''Modal Analysis of a Distributed Parameter Rotating Beam,'' J. Sound Vib., **122**, No. 1, pp. 119–130.

[3] Katz, R., Lee, C. W., Ulsoy, A. G., and Scott, R. A., 1988, ''Dynamic Responses of a Rotating Shaft Subjected to a Moving Load,'' J. Sound Vib., **122**, No. 1, pp. 131–148.

[4] Zu, J. W., and Han, R. P. S., 1992, ''Natural Frequencies and Normal Modes of a Spinning Timoshenko Beam With General Boundary Conditions,'' ASME J. Appl. Mech., **59**, pp. S197–S203.

[5] Tabarrok, B., and Rimrott, F. P. J., 1994, *Variational Methods and Complementary Formulations in Dynamics*, Kluwer, Dordrecht, The Netherlands.

Penetration Experiments With Limestone Targets and Ogive-Nose Steel Projectiles

D. J. Frew
Assoc. Mem. ASME, Waterways Experiment Station, Vicksburg, MS 39180-6199

M. J. Forrestal
Fellow ASME, Sandia National Laboratories, Albuquerque, NM 87185-0303

S. J. Hanchak
University of Dayton Research Institute, Dayton, OH 45469-0182

We conducted three sets of depth-of-penetration experiments with limestone targets and 3.0 caliber-radius-head (CRH), ogive-nose steel rod projectiles. The ogive-nose rod projectiles with length-to-diameter ratios of ten were machined from 4340 R_c 45 and Aer Met 100 R_c 53 steel, round stock and had diameters and masses of 7.1 mm, 0.020 kg; 12.7 mm, 0.117 kg; and 25.4 mm, 0.931 kg.

Contributed by the Applied Mechanics Division of THE AMERICAN SOCIETY OF MECHANICAL ENGINEERS for publication in the ASME JOURNAL OF APPLIED MECHANICS. Manuscript received by the ASME Applied Mechanics Division, Nov. 29, 1999; final revision, May 10, 2000. Associate Technical Editor: I. M. Daniel.

Powder guns or a two-stage, light-gas gun launched the projectiles at normal impacts to striking velocities between 0.4 and 1.9 km/s. In addition, we present an analytical penetration equation that described the target resistance by its density and a strength parameter determined from depth of penetration versus striking velocity data. [S0021-8936(01)00201-X]

Introduction

Several authors have written review articles that discuss the many analytical, computational, and experimental methods used to study the broad field of penetration mechanics ([1–5]). The responses of the projectiles and targets depend strongly on the problem geometry, materials, and impact conditions. Because many penetration mechanisms are possible, experimental observations usually precede and guide analytical or computational models. For this study, post-test observations showed a conical entry crater with a depth of two or more projectile diameters followed by a circular penetration channel or tunnel with nearly the projectile diameter. For recent penetration studies with 6061-T6511 aluminum targets ([6,7]) we could obtain post-test radiographs of the penetration channels. However, we could obtain post-test observations of the limestone penetration channels only after the targets were split with the techniques used by stone masons. The projectiles recovered from the targets had small mass losses caused by abrasion, but the overall nose shapes before and after penetration looked very similar. We previously observed similar post-test, target channels and abraded projectiles with our studies on concrete targets ([8,9]). However, the concrete targets abraded the nose tips more severely than the limestone targets.

Based on penetration data sets with three projectile scales, we present an analytical penetration equation that describes target resistance by a parameter determined from penetration depth versus striking velocity data. Our limestone penetration equation is similar to that previously derived for concrete targets ([10]). However, for limestone targets, we observed a noticeable decrease in the target resistance parameter as the projectile diameters increased. So for the limestone targets, the target resistance parameter is equal to a constant term plus a term that depends on the projectile diameter. We hypothesize that the penetration equation will be reasonably accurate for larger scale projectiles, but data from much more expensive field tests must be obtained to confirm our hypothesis.

The limestone targets were quarried and cut by the Elliot Stone Company.[1] In the rock mechanics literature, this particular limestone is often called Salem, Indiana, or Bedford limestone. For this study, we conducted unconfined compression tests and some triaxial compression tests on samples cored from representative blocks and from individual targets before the penetration tests. Material properties from our targets are nearly the same as those reported by Fossum, Senseny, Pfeifle, and Mellegard [11].

As previously mentioned, our penetration equation contains a target strength constant that is determined from penetration depth versus striking velocity data. While this methodology provides an accurate and convenient engineering equation, the detailed response mechanisms for the target are not modeled. The authors are not aware of any rigorous target models for rock penetration problems, but Lagrangian computational models that use adaptive meshing techniques have shown promise for brittle ceramic targets ([12,13]). Detailed computational approaches that model target responses also require a broad array of quasi-static and dynamic material properties data. For limestone, examples of some materials experiments and data include (1) quasi-static, triaxial compression experiments ([11]), (2) split Hopkinson bar experiments ([14–16]), (3) shock wave studies ([17]), (4) dynamic tensile failure with planar-impact techniques ([18,19]), and (5) compression-shear loading with plate impact experiments ([20]). Data from other experimental techniques may also be required for a careful target analysis.

In the next sections, we present the penetration model, describe the experiments, and present our results and conclusions.

Penetration Model

For both limestone and concrete targets, post-test observations showed a conical entry crater with a depth of two or more projectile diameters followed by a circular channel or tunnel with nearly the projectile diameter. The limestone penetration equations are similar to the previously published concrete penetration equations. From Forrestal, Altman, Cargile, and Hanchak [10], depth of penetration P for an ogive-nose projectile and a concrete target is given by

$$P=\frac{m}{2\pi a^2\rho N}\ln\left(1+\frac{N\rho V_1^2}{R}\right)+4a,\quad P>4a \tag{1a}$$

$$N=\frac{8\psi-1}{24\psi^2},\quad V_1^2=\frac{mV_s^2-4\pi a^3R}{m+4\pi a^3N\rho} \tag{1b}$$

in which the ogive-nose rod projectile is described by mass m, shank radius a, and caliber-radius-head ψ. The target is described by density ρ and the target strength constant R. The strength constant is determined from

$$R=\frac{N\rho V_s^2}{\left(1+\dfrac{4\pi a^3N\rho}{m}\right)\exp\left[\dfrac{2\pi a^2(P-4a)N\rho}{m}\right]-1} \tag{2}$$

where V_s is striking velocity. For a set of experiments, we hold all parameters constant and vary striking velocity. From each experiment, we measure striking velocity V_s and penetration depth P, so R can be determined from (2) for each experiment. We then take the average value of R from the data set and compare the prediction from (1) with the measured values of V_s and P. For this study with limestone targets, ogive-nose steel rod projectiles with 7.1, 12.7, and 25.4-mm diameters and a length-to-diameter ratio of ten have values of $R=913$, 787, and 693 MPa, respectively. Thus, the target resistance decreases as the projectile shank diameter increases. We found that for these limestone targets

$$R=K+k(2a_o/2a) \tag{3}$$

in which K and k are constants obtained from data fits, $2a_o$ is a reference projectile diameter, and $2a$ is the projectile diameter. We show later that with $K=607$ MPa, $k=86$ MPa, and $2a_o=25.4$ mm, we accurately recover the measured values of R for each of the three data sets.

In summary, the procedure used to calculate R from penetration depth data for a fixed projectile is the same for concrete or limestone targets. However, for limestone targets, R depends on the projectile shank diameter. Thus, we can use the penetration equations (1*a*) and (1*b*) for limestone when R is given by (3).

Experiments

We conducted three sets of penetration experiments (a total of 30 experiments) with ogive-nose steel rod projectiles and limestone targets. All projectiles had a total length-to-diameter ratio of ten and 3.0 caliber-radius-head (CRH) nose shapes. The shank diameters and masses for each of the three sets of experiments were 7.1 mm, 0.020 kg; 12.7 mm, 0.117 kg; and 25.4 mm, 0.931 kg.

Limestone Targets. The limestone targets were quarried and cut by the Elliot Stone Company of Bedford, IN. We obtained the targets in three batches from nearby sites. Nominal material properties for the three target batches are given in Table 1 and show minimal variations among the batches. In addition, we conducted

[1]Elliot Stone Company, 3326 Mitchell Road, Bedford, IN 47421.

Table 1 Nominal material properties for the limestone targets

Batch number	Density ρ (Mg/m^3)	Water content w (%)	Porosity n (%)	Compressive strength σ_{cf} (MPa)
1	2.32	0.16	14.4	58
3	2.30	0.16	15.1	63
4	2.31	0.11	14.8	61

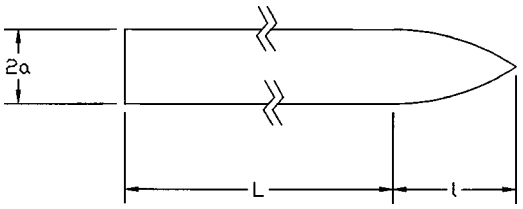

Fig. 1 Projectile geometry

several triaxial compression tests ([21,22]) on samples from the three target batches and found the brittle to ductile transition confining pressure to be about 50 MPa.

The 12.7-mm-Diameter, 0.117 kg, 3.0 CRH Projectiles. Our first set of experiments was conducted with steel projectiles machined from 4340 R_c 45 ([23]) round stock. Figure 1 shows the projectile geometry, and for this set of experiments $2a=12.7$ mm, $L=106$ mm, and $l=21$ mm. The target impact surface was 0.51 m square, and the target lengths and other data are given in Table 2. The sides and bottom of the targets were surrounded by 0.10-m-thick concrete placed between a steel form and the limestone. Six unconfined compression tests were conducted with 51-mm-diameter, 108-mm-long samples cored from a representative limestone block from Batch 1 and the average strength was $\sigma_{cf}=58$ MPa.

A 32-mm-diameter powder gun launched the 0.117 kg projectiles to the striking velocities recorded in Table 2. An additional experiment was conducted at $V_s=1605$ m/s, but the trajectory was

Table 2 Penetration data for the 12.7-mm-diameter 4340 R_c 44–45, 0.117 kg, 3.0 CRH projectiles. For ptich and yaw: *D*=down, *U*=up, *R*=right, *L*=left.

Shot, batch numbers	Target length (m)	Striking velocity V_s (m/s)	Pitch, yaw (deg.)	Penetration depth P(m)	Projectile mass loss (%)	R (MPa)
1-0370, 1	0.61	459	1.9D, 3.0L	0.141	0.16	733
1-0371, 1	0.61	608	1.0U, 1.0R	0.232	0.24	734
1-0372, 1	0.91	853	0, 0	0.362	0.96	875
1-0377, 1	0.91	956	0, 0.3L	0.523	1.29	719
1-0373, 1	0.91	1134	1.0U, 1.9R	0.562	2.59	930
1-0376, 1	1.22	1269	0, 0	0.812	3.87	745
1-0375, 1	1.22	1404	0, 0.7R	0.924	5.25	775
1-0374, 1	1.22	1502	0.7U, 0	1.017	5.90	783

Table 3 Penetration data for the 7.1-mm-diameter 4340 R_c 44–46 or Aer Met 100 R_c 53 (shots 4-1847 and 4-1846), 0.0205 kg, 3.0 CRH projectiles. For pitch and yaw: *D*=down, *U*=up, *R*=right, *L*=left.

Shot, batch numbers	Target length (m)	Striking velocity V_s (m/s)	Pitch, yaw (deg.)	Penetration depth P(m)	Projectile mass loss (%)	R (MPa)	Compressive strength σ_{cf} (MPa)
1-0422, 3	0.30	497	0, 0.75R	0.067	0.34	1033	
1-0418, 3	0.61	597	0.5U, 0	0.105	0.34	895	64.7
1-0419, 3	0.61	787	0, 1.25R	0.165	0.78	937	
1-0420, 3	0.61	1037	0.75U, 0.5R	0.271	2.11	927	
4-1835, 3	1.02	1365	2.0D, 1.6R	0.430	4.90	926	58.2
4-1836, 3	1.02	1516	0.9U, 1.1R	0.516	7.34	903	
1-0439, 1	0.46	795	0.5U, 0	0.178	0.83	877	60.1
1-0440, 1	0.61	1060	0.25U, 0.5R	0.294	2.49	877	60.3
1-0441, 1	0.61	1230	0, 0.25R	0.392	3.76	837	55.7
4-1845, 1	1.02	1340	1.75D, 1.0L	0.437	4.84	870	57.5
4-1847, 3	1.02	1266	1.0D, 1.5R	0.379	4.59	925	63.8
4-1846, 3	1.02	1674	0.5U, 0	0.581	10.85	944	63.9

Table 4 Penetration data for the 25.4-mm-diameter 4340 R_c 45–46, 0.931 kg, 3.0 CRH projectiles. For pitch and yaw: *D*=down, *U*=up, *R*=right, *L*=left.

Shot, batch numbers	Target length (m)	Striking velocity V_s (m/s)	Pitch, yaw (deg.)	Penetration depth P(m)	Projectile mass loss (%)	R (MPa)	Compressive strength σ_{cf} (MPa)
LROD99-1, 4	0.61	407	0.4D, 0.5L	0.26	0	617	56.2
LROD99-2, 4	0.76	566	0.6U, 0	0.39	0.1	769	61.9
LROD99-3, 4	1.07	800	0.6D, 0.1L	0.79	0.3	693	66.7
LROD99-6, 4	1.52	917	—, 0.3R	1.02	1.1	681	59.8
LROD99-7, 4	1.98	1177	0, 0.3R	1.50	2.8	705	61.2

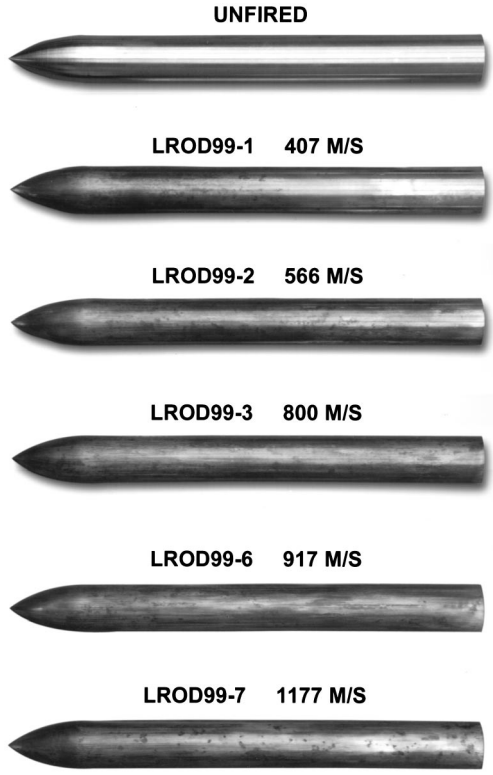

Fig. 2 Post-test photographs of the 25.4-mm-diameter projectiles

curved and the projectile exited the side of the target at a depth of about 0.65 m. The projectiles were fitted with sabots and obturators that separated from the projectiles before impact. Four laser diode systems measured striking velocities and orthogonal radiographs measured pitch and yaw angles. The target resistance R was calculated from (2) for each experiment and recorded in Table 2. The average target resistance parameter for this set of experiments is $R=787$ MPa.

The 7.1-mm-Diameter 0.020 kg, 3.0 CRH Projectiles. Our second set of experiments was conducted with steel projectiles machined from both 4340 R_c 45 and Aer Met 100 R_c 53 ([24]) round stock. Figure 1 shows the projectile geometry, and for this set of experiments $2a=7.11$ mm, $L=59.3$ mm, and $l=11.8$ mm. A 20-mm-powder gun launched the 0.020 kg projectiles to striking velocities of 1230 m/s. For the larger striking velocities recorded in Table 3, a two-stage 50/20 mm light-gas gun launched the projectiles. The same target geometries and ballistics measurements as those described for the 12.7-mm-diameter 0.117 kg projectiles were used for this set of experiments.

For this second set of experiments, we performed unconfined compression tests on two samples cored from the targets. The compressive strengths listed in Table 3 are the average of two unconfined compression tests conducted with 50-mm-diameter 108-mm-long cores. In addition, we conducted penetration experiments from both Batch 1 and Batch 3 limestone targets to compare results from the two batches. We show later negligible differences in the penetration data from both batches. The average target resistance parameter of this set of experiments is $R=913$ MPa.

We also conducted an experiment with a 4340 R_c 45 projectile at $V_s=1649$ m/s. That projectile severely bent and turned within the target. Table 3 shows two experiments conducted with Aer Met 100 R_c 53 projectiles. Shot 4-1846 with a striking velocity of 1674 m/s had a nearly straight trajectory. We then conducted experiments at $V_s=1749$, 1826, and 1863 m/s with Aer Met 100 R_c 53 projectiles and these projectiles severely bent and turned within the targets. Piekutowski, Forrestal, Poormon, and Warren [7] discusses in detail the better performance of the Aer Met 100 R_c 53 projectiles.

The 25.4-mm-diameter 0.931 kg, 3.0 CRH Projectiles. Our third set of experiments was conducted with steel projectiles ma-

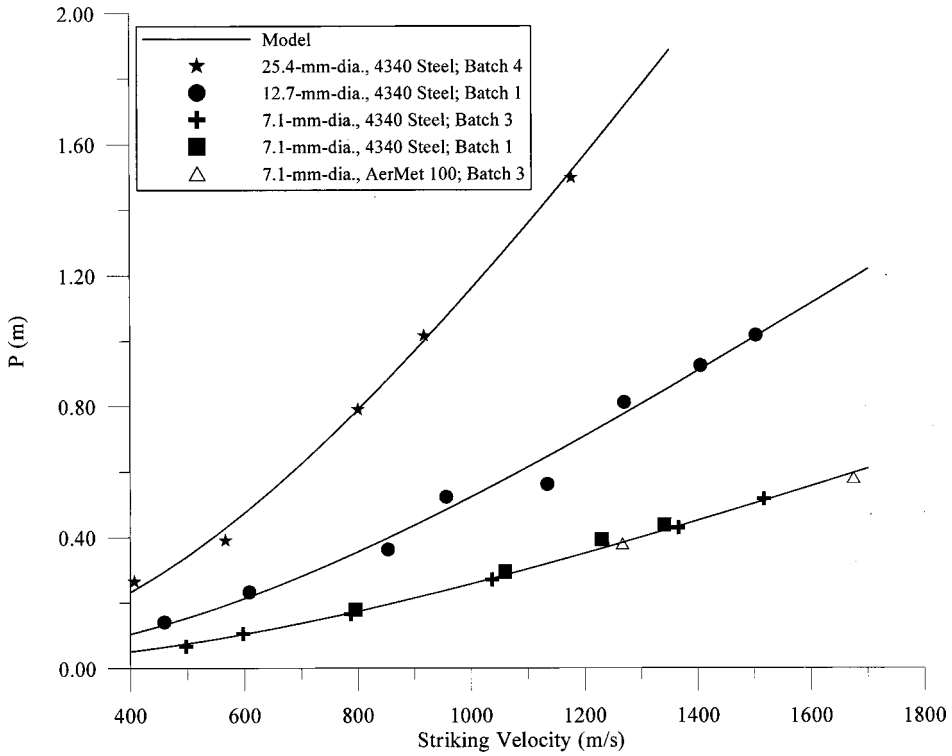

Fig. 3 Data and model predictions for the limestone targets

chined from 4340 R_c 45 round stock. Figure 1 shows the projectile geometry, and for this set of experiments $2a=25.4$ mm, $L=212$ mm, and $l=42$ mm. The target impact surface was 1.02-m square and the target lengths are given in Table 4. The sides and bottom of the targets were surrounded by 0.10-m-thick concrete placed between a steel form and the limestone. An 83-mm powder gun launched the 0.931 kg projectiles to the striking velocities recorded in Table 4. The same experimental methods used for the other data sets were also used to obtain the results given in Table 4. Data in Table 4 were limited to $V_s=1177$ m/s because of the size and mass of the targets. The average value of R for this set of experiments was $R=693$ MPa.

Results and Discussion

As previously discussed, post-test target observations for the experiments summarized in Tables 2, 3, and 4 showed a conical entry crater with a depth of two or more projectile diameters followed by a circular penetration tunnel with nearly the projectile diameter. However, we made post-test observations only after the targets were split with the techniques used by stone masons. Figure 2 shows post-test photographs of the 25.4-mm-diameter projectiles, and mass losses are given in Table 4. These recovered projectiles lost mass caused by abrasion, but the nose shapes before and after penetration have similar shapes. Post-test projectiles from the other data sets (Tables 2 and 3) had shapes similar to those shown in Fig. 2.

Figure 3 shows depth of penetration P versus striking velocity V_s for the data in Tables 2, 3, and 4. For the model, we use the average value of R calculated from (2) for the experiments in each data set. For the 7.1, 12.7, and 25.4-mm-diameter projectiles, the average target resistance parameter is $R=913$, 787, and 693 MPa, respectively. For projectile diameters not tested in this study, we recommend (3) be used to calculate R. Equation (3) with $K=607$ MPa, $k=86$ MPa, and $2a_o=25.4$ mm accurately recover the measured values of R from each of the three data sets. We hypothesize that the penetration equations ((1) and (3)) for this limestone target will be reasonably accurate for larger scale projectiles, but data from much more expensive field tests with larger diameter projectiles must be obtained to confirm our hypothesis.

Summary

We conducted sets of penetration experiments into limestone targets with three scales of geometrically similar projectiles. The ogive-nose rod projectiles with a length-to-diameter ratio of ten were machined from 4340 R_c 45 and Aer Met 100 R_c 53 steel, round stock and had diameters and masses of 7.1 mm, 0.020 kg; 12.7 mm, 0.117 kg; and 25.4 mm, 0.931 kg. For the 4340 R_c 45 and Aer Met 100 R_c 53 steel projectiles, penetration depth increased as striking velocity increased to 1500 and 1700 m/s, respectively. For larger striking velocities, the projectiles bent during penetration without nose erosion, deviated from the shot line, and exited the sides of the target or turned severely in the target.

Based on data sets with these three projectile scales, we present an analytical penetration equation based on a target strength parameter that is determined from penetration depth versus striking velocity data. We show that the target resistance parameter depends on the projectile shank diameter and present an equation that describes this diameter dependence. We hypothesize that the penetration equations for this limestone target will give accurate predictions for larger scale projectile, but data from much more expensive field tests with larger diameter projectiles must be obtained to confirm our hypothesis.

Acknowledgments

This work was supported by the United States Department of Energy under Contract DE-AC04-94AL85000, the Joint DoD/DOE Munitions Technology Development Program, and the U.S. Army Corps of Engineers Hardened Structures Research Programs (AT22 and AT40).

References

[1] Backman, M. E., and Goldsmith, W., 1978, ''The Mechanics of Penetration of Projectiles Into Targets,'' Int. J. Eng. Sci., **16**, pp. 1–99.

[2] Anderson, C. E., and Bodner, S. R., 1988, ''Ballistic Impact: The Status of Analytical and Numerical Modeling,'' Int. J. Impact Eng., **7**, pp. 9–35.

[3] Hohler, V., and Stilp, A. J., 1990, ''Long-Rod Penetration Mechanics,'' *High Velocity Impact Dynamics*, J. A. Zukas, ed., John Wiley and Sons, New York, Chapter 5.

[4] Recht, R., 1990, ''High Velocity Impact Dynamics: Analytical Modeling of Plate Penetration Dynamics,'' *High Velocity Impact Dynamics*, J. A. Zukas, ed., John Wiley and Sons, New York, Chapter 7.

[5] Corbett, G. G., Reid, S. R., and Johnson, W., 1996, ''Impact Loading of Plates and Shells by Free-Flying Projectiles: A Review,'' Int. J. Impact Eng., **18**, pp. 141–230.

[6] Warren, T. L., and Forrestal, M. J., 1998, ''Effects of Strain Hardening and Strain-Rate Sensitivity on the Penetration of Aluminum Targets With Spherical-Nosed Rods,'' Int. J. Solids Struct., **35**, Nos. 28–29, pp. 3737–3753.

[7] Piekutowski, A. J., Forrestal, M. J., Poormon, K. L., and Warren, T. L., 1999, ''Penetration of 6061-T6511 Aluminum Targets by Ogive-Nose Steel Projectiles With Striking Velocities Between 0.5 and 3.0 km/s,'' Int. J. Impact Eng., **23**, pp. 723–734.

[8] Forrestal, M. J., Frew, D. J., Hanchak, S. J., and Brar, N. S., 1996, ''Penetration of Grout and Concrete Targets With Ogive-Nose Steel Projectiles,'' Int. J. Impact Eng., **18**, No. 5, pp. 465–476.

[9] Frew, D. J., Hanchak, S. J., Green, M. L., and Forrestal, M. J., 1998, ''Penetration of Concrete Targets With Ogive-Nose Steel Rods,'' Int. J. Impact Eng., **21**, No. 6, pp. 489–497.

[10] Forrestal, M. J., Altman, B. S., Cargile, J. D., and Hanchak, S. J., 1994, ''An Empirical Equation for Penetration Depth of Ogive-Nose Projectiles Into Concrete Targets,'' Int. J. Impact Eng., **15**, No. 4, pp. 395–405.

[11] Fossum, A. F., Senseny, P. E., Pfeifle, T. W., and Mellegard, K. D., 1995, ''Experimental Determination of Probability Distributions for Parameters of a Salem Limestone Cap Plasticity Model,'' Mech. Mater., **21**, pp. 119–137.

[12] Ortiz, M., 1996, ''Computational Micromechanics,'' Comput. Mech., **18**, pp. 321–338.

[13] Camacho, G. T., and Ortiz, M., 1997, ''Adaptive Lagrangian Modelling of Ballistic Penetration of Metallic Targets,'' Comput. Meth., Appl. Eng., **142**, pp. 269–301.

[14] Green, S. J., and Perkins, R. D., 1972, ''Uniaxial Compression Tests at Varying Strain Rates on Three Geologic Materials,'' *Proc. 10th Symp. Rock Mechanics, Inst. Mining Metallurgical and Petroleum Engrs.*, K. E. Gray, ed., AIME, New York, pp. 35–54.

[15] Lindholm, U. S., Yeakley, L. M., and Nagy, A., 1974, ''The Dynamic Strength and Fracture Properties of Dresser Basalt,'' Int. J. Rock Mech. Min. Sci. Geomech. Abstr., **II**, pp. 181–191.

[16] Lipkin, J., Grady, D. E., and Campbell, J. D., 1977, ''Dynamic Flow and Fracture of Rock in Pure Shear,'' *Proc. 18th U.S. Symp. Rock Mechanics*, F. Wang and G. B. Clark, eds., Colorado School of Mines Press, Golden, Co, pp. 3 B2–1, 3 B2–7.

[17] Larson, D. B., and Anderson, G. D., 1979, ''Plane Shock Wave Studies of Porous Geological Media,'' J. Geophys. Res., **84**, No. B9, pp. 4592–4600.

[18] Grady, D. E., and Hollenbach, R. E., 1979, ''Dynamic Fracture Strength of Rock,'' Geophys. Res. Lett., **6**, No. 2, pp. 73–76.

[19] Ahrens, T. J., and Rubin, A. M., 1993, ''Impact-Induced Tensional Failure in Rock,'' J. Geophys. Res., **98**, No. E1, pp. 1185–1203.

[20] Aidun, J. B., and Gupta, Y. M., 1995, ''Shear and Compression Waves in Shocked Calcium Carbonate,'' J. Geophys. Res., **100**, No. B2, pp. 1955–1980.

[21] Farmer, I., 1983, *Engineering Behavior of Rocks*, 2nd Ed., Chapman and Hall, New York.

[22] Jaeger, J. C., and Cook, N. G. W., 1979, *Fundamentals of Rock Mechanics*, 3rd Ed., Chapman and Hall, New York.

[23] Brown, W. F., Mindlin, H., and Ho, C. Y., 1996, *Aerospace Structural Metals Handbook*, Vol. 1, Code 1206, CINDAS/USAF CRDA Handbooks Operation, Purdue University, West Lafayette, IN.

[24] Dahl, J., 1991, ''Aer Met 100—An Advanced Steel for the Aerospace Industry,'' Adv. Mat. Tech. Int., pp. 40–45.

Eccentric Crack in a Piezoelectric Strip Under Electromechanical Loading

Jeong Woo Shin
Researcher, Korea Aerospace Research Institute,
52 Oun-dong, Yusong-gu, Taejon 306-333, Korea

Soon Man Kwon
Graduate Student

Kang Yong Lee[1]
Professor

Department of Mechanical Engineering, Graduate School,
Yonsei University, Seoul 120-749, Korea

1 Introduction

With an increasingly wide application media in engineering, the study on the crack problem in piezoelectric media has received much interest. In this paper, we apply the theory of linear piezoelectricity to the electroelastic problem of a finite eccentric crack off the center line in a piezoelectric ceramic strip under antiplane shear loading. The continuous crack boundary condition is adopted. By using integral transform techniques, the problem is reduced to the solution of a Fredholm integral equation of the second kind, which is obtained from two pairs of dual integral equations. Numerical results for the energy release rate are shown graphically.

2 Problem Statement and Method of Solution

Consider a piezoelectric medium in the form of an infinitely long strip containing a finite eccentric crack off the center line parallel to the edges subjected to the combined antiplane mechanical and in-plane electric loads. A set of Cartesian coordinates (x,y,z) is attached to the center of the crack. The total thickness of the strip is $2h(=h_1+h_2)$, where $h_1(=h-e)$ is the distance between the top surface of the strip and the crack plane and $h_2(=h+e)$ is that between the bottom surface of the strip and the crack plane. e denotes the distance from the center line of the strip to the crack plane. The crack is situated along the virtual interface $(-a\leqslant x\leqslant a,\ y=0)$. Because of the assumed symmetry in geometry and loading, it is sufficient to consider the problem for $0\leqslant x<\infty$ only. Antiplane governing equations are simplified to

$$c_{44}\nabla^2 w^{(i)}+e_{15}\nabla^2\phi^{(i)}=0, \tag{1}$$

$$e_{15}\nabla^2 w^{(i)}-d_{11}\nabla^2\phi^{(i)}=0, \tag{2}$$

where $\nabla^2=\partial^2/\partial x^2+\partial^2/\partial y^2$ is the two-dimensional Laplace operator, $w^{(i)}$, $\phi^{(i)}$ $(i=1,2)$, c_{44}, d_{11}, and e_{15} are the out-of-plane displacement, the electric potential, the elastic modulus measured in a constant electric field, the dielectric permittivity measured at a constant strain, and the piezoelectric constant, respectively. Superscript i $(i=1,2)$ stands for upper and lower regions, respectively. The boundary conditions are written as follows:

$$\sigma_{yz}^{(i)}(x,0)=0, \quad (0\leqslant x<a), \tag{3}$$

$$w^{(1)}(x,0^+)=w^{(2)}(x,0^-), \quad (a\leqslant x<\infty), \tag{4}$$

$$D_y^{(1)}(x,0^+)=D_y^{(2)}(x,0^-), \quad (0\leqslant x<a), \tag{5}$$

$$E_x^{(1)}(x,0^+)=E_x^{(2)}(x,0^-), \quad (0\leqslant x<a), \tag{6}$$

$$\phi^{(1)}(x,0^+)=\phi^{(2)}(x,0^-), \quad (a\leqslant x<\infty), \tag{7}$$

$$\begin{aligned}&\sigma_{yz}^{(1)}(x,0^+)=\sigma_{yz}^{(2)}(x,0^-) \quad (a\leqslant x<\infty),\\ &D_y^{(1)}(x,0^+)=D_y^{(2)}(x,0^-), \quad (a\leqslant x<\infty).\end{aligned} \tag{8}$$

$$\begin{aligned}\text{Case 1: }&\sigma_{yz}^{(1)}(x,h_1)=\sigma_{yz}^{(2)}(x,-h_2)=\tau_0,\\ &D_y^{(1)}(x,h_1)=D_y^{(2)}(x,-h_2)=D_0,\end{aligned} \tag{9}$$

$$\begin{aligned}\text{Case 2: }&\gamma_{yz}^{(1)}(x,h_1)=\gamma_{yz}^{(2)}(x,-h_2)=\gamma_0,\\ &E_y^{(1)}(x,h_1)=E_y^{(2)}(x,-h_2)=E_0,\end{aligned} \tag{10}$$

$$\begin{aligned}\text{Case 3: }&\sigma_{yz}^{(1)}(x,h_1)=\sigma_{yz}^{(2)}(x,-h_2)=\tau_0,\\ &E_y^{(1)}(x,h_1)=E_y^{(2)}(x,-h_2)=E_0,\end{aligned} \tag{11}$$

$$\begin{aligned}\text{Case 4: }&\gamma_{yz}^{(1)}(x,h_1)=\gamma_{yz}^{(2)}(x,-h_2)=\gamma_0,\\ &D_y^{(1)}(x,h_1)=D_y^{(2)}(x,-h_2)=D_0,\end{aligned} \tag{12}$$

where $\sigma_{yz}^{(i)}$, $\gamma_{yz}^{(i)}$, $D_y^{(i)}$, and $E_j^{(i)}$ $(j=x,y)$ are the shear stress, the shear strain, the electric displacements, and the electric fields, respectively, and τ_0, D_0, γ_0, and E_0 are a uniform shear stress, displacement, shear strain, and electric field, respectively. A Fourier transform is applied to Eqs. (1) and (2), and the results are

$$w^{(i)}(x,y)=\frac{2}{\pi}\int_0^\infty\{A_1^{(i)}(s)\cosh(sy)+A_2^{(i)}(s)\sinh(sy)\}\times\cos(sx)ds+a_0y, \tag{13}$$

$$\phi^{(i)}(x,y)=\frac{2}{\pi}\int_0^\infty\{B_1^{(i)}(s)\cosh(sy)+B_2^{(i)}(s)\sinh(sy)\}\times\cos(sx)ds-b_0y, \tag{14}$$

where $A_j^{(i)}$, $B_j^{(i)}$ $(j=1,2)$ are the unknowns to be solved. a_0,b_0 are real constants, which will be determined from the edge loading conditions. Applying Eqs. (8)–(12), and considering Eqs. (3)–(7), we obtain the following two simultaneous dual integral equations:

$$\begin{aligned}&\int_0^\infty sF(s)\left[M_A(s)+\frac{e_{15}}{c_{44}}M_B(s)\right]\cos(sx)ds=\frac{\pi}{2}\frac{c_0}{c_{44}}, \quad (0\leqslant x<a),\\ &\int_0^\infty M_A(s)\cos(sx)ds=0, \quad (a\leqslant x<\infty),\end{aligned} \tag{15}$$

$$\begin{aligned}&\int_0^\infty sM_B(s)\sin(sx)ds=0, \quad (0\leqslant x<a),\\ &\int_0^\infty M_B(s)\cos(sx)ds=0, \quad (a\leqslant x<\infty),\end{aligned} \tag{16}$$

where

$$2M_A(s)=A_1^{(1)}(s)-A_1^{(2)}(s), \quad 2M_B(s)=B_1^{(1)}(s)-B_1^{(2)}(s), \tag{17}$$

$$F(s)=\tanh(sh)-\frac{2\sinh^2(se)}{\sinh(2sh)}, \tag{18}$$

[1]To whom correspondence should be addressed.

Contributed by the Applied Mechanics Division of THE AMERICAN SOCIETY OF MECHANICAL ENGINEERS for publication in the ASME JOURNAL OF APPLIED MECHANICS. Manuscript received by the ASME Applied Mechanics Division, Jan. 19, 2000; final revision, Apr. 20, 2000. Associate Technical Editor: D. Kouris.

$$c_0 = c_{44}a_0 - e_{15}b_0, \tag{19}$$

$$= \tau_0, \quad \text{Cases 1 and 3,} \tag{20a}$$

$$= c_{44}\gamma_0 - e_{15}E_0, \quad \text{Case 2,} \tag{20b}$$

$$= \frac{(c_{44}d_{11} + e_{15}^2)\gamma_0 - e_{15}D_0}{d_{11}}, \quad \text{Case 4.} \tag{20c}$$

To solve the two sets of dual integral equations, we define $M_A(s)$ and $M_B(s)$ as follows:

$$M_A(s) \equiv \frac{\pi}{2}\frac{c_0 a^2}{c_{44}}\int_0^1 \sqrt{\xi}\Psi(\xi)J_0(sa\xi)d\xi,$$
$$M_B(s) \equiv \int_0^1 \sqrt{\xi}\Phi(\xi)J_0(sa\xi)d\xi, \tag{21}$$

where $J_0(sa\xi)$ is the zero-order Bessel function of the first kind. Inserting Eq. (21) into Eqs. (15) and (16), we can find that $\Phi(\xi)=0$ and $\Psi(\xi)$ is given by a Fredholm integral equation of the second kind in the form

$$\Psi(\xi) + \int_0^1 K(\xi,\eta)\Psi(\eta)d\eta = \sqrt{\xi}, \tag{22}$$

where

$$K(\xi,\eta) = \sqrt{\xi\eta}\int_0^\infty s\{F(s/a)-1\}J_0(s\eta)J_0(s\xi)ds. \tag{23}$$

Extending the traditional concept of stress intensity factor to other field variables ([1]), we have

$$K^T = c_0\sqrt{\pi a}\Psi(1), \quad K^S = K^T/c_{44}, \quad K^D = e_{15}K^T/c_{44}, \quad K^E = 0, \tag{24}$$

where K^T, K^S, K^D, and K^E are stress intensity, strain intensity, electric displacement intensity, and electric field intensity factor, respectively. Evaluating the energy release rate G obtained by Pak [1], we obtain

$$G = \frac{K^T K^S - K^D K^E}{2} = \frac{\pi a}{2c_{44}}c_0^2\Psi^2(1). \tag{25}$$

3 Numerical Results and Discussion

From Eq. (24), it is noted that the uniform electric load has no influence on the field singularities, and the electric displacement intensity factor depends on the material constants and the applied mechanical load, τ_0 but not on the applied electric loads, D_0 and E_0. The results coincide with the ones of Kwon and Lee [2] and Gao and Fan [3]. Figure 1 displays the normalized energy release rate G/G_∞ versus the a/h with various e/h values. G/G_∞ increases with increase of the a/h and e/h ratios. The normalized energy release rate G/G_{cr} of a PZT-5H ceramic is shown in Fig. 2 with the variation of the applied electric field E_0 and the a/h ratio for a crack length of $2a=0.02$ m and $\gamma_0 = 9.5\times10^{-5}$ (Case 2) in cases of $e/h=0.0$ and $e/h=0.5$. As the magnitude of electric field increases from zero, G increases or decreases according to the direction of the load. But once the minimum value of G is reached, further increase of the electrical load increase G continuously. G increase with increase of the e/h ratio. It can be shown that similar results are obtained in Case 4.

4 Conclusions

The normalized energy release rate increases when the a/h and e/h ratios increase. The energy release rate is dependent on the electric loading only under constant strain loading and independent of it under constant stress loading. In constant strain loadings, the minimum normalized energy release rate can exist with the variation of electrical load but has always positive values.

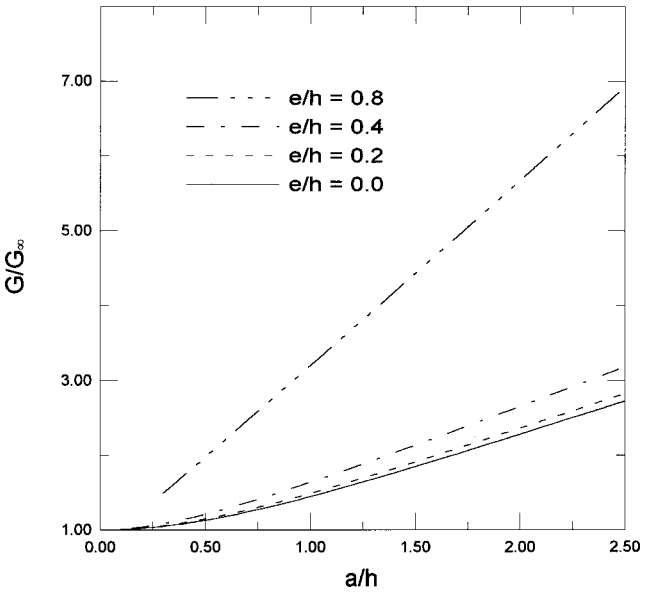

Fig. 1 Energy release rate G/G_∞ versus a/h with various e/h values

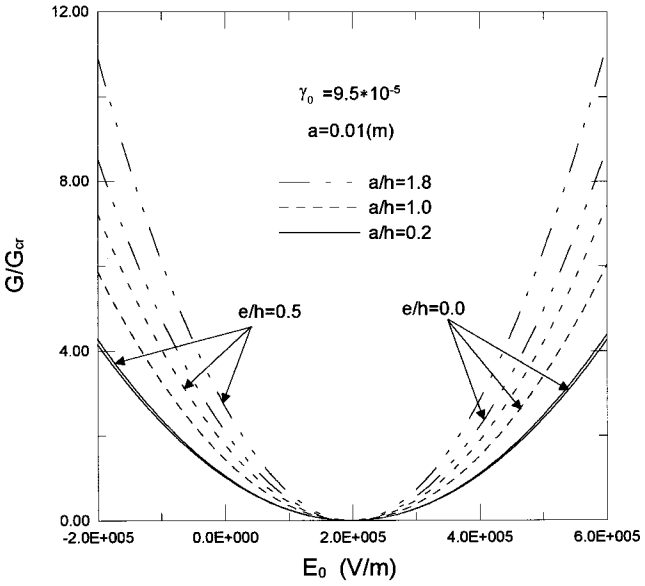

Fig. 2 Energy release rate of PZT-5H (Case 2) with various e/h values

Acknowledgments

The authors are grateful for the support provided by the Brain Korea 21 Project and a grant from the Korea Science & Engineering Foundation (KOSEF) and Safety and Structural Integrity Research Center at the Sungkyunkwan University.

References

[1] Pak, Y. E., 1990, ''Crack Extension Force in a Piezoelectric Materials,'' ASME J. Appl. Mech., **57**, pp. 647–653.

[2] Kwon, S. M., and Lee, K. Y., 2000, ''Analysis of Stress and Electric Fields in a Rectangular Piezoelectric Body With a Center Crack Under Anti-plane Shear Loading,'' Int. J. Solids Struct., **37**, pp. 4859–4869.

[3] Gao, C. F., and Fan, W. X., 1999, ''A General Solution for the Plane Problem in Piezoelectric Media With Collinear Crack,'' Int. J. Eng. Sci., **37**, pp. 347–363.